Available online at www.sciencedirect.com
ScienceDirect
Journal of Sound and Vibration 310 (2008) 260–286
JOURNAL OF SOUND AND VIBRATION
www.elsevier.com/locate/jsvi

Computational modelling of string–body interaction for the violin family and simulation of wolf notes

O. Inácio[a,*], J. Antunes[b], M.C.M. Wright[c]

[a]*Instituto Politécnico do Porto, ESMAE, Musical Acoustics Laboratory, Rua da Alegria, 503, 4000-045 Porto, Portugal*
[b]*Instituto Tecnológico e Nuclear, Applied Dynamics Laboratory ITN/ADL, Estrada Nacional 10, 2686-953 Sacavém Codex, Portugal*
[c]*Institute of Sound and Vibration Research, University of Southampton, Southampton S017 1BJ, UK*

Received 5 August 2006; received in revised form 12 July 2007; accepted 30 July 2007
Available online 3 October 2007

Abstract

Most theoretical studies of bowed-string instruments deal with isolated strings, pinned on fixed supports. In others, the instrument body dynamics have been accounted by using extremely simplified models of the string–body interaction through the instrument bridge. Such models have, nevertheless, been instrumental to the understanding of a very common and musically undesirable phenomenon known as the *wolf note*—a strong beating interplay between string and body vibrations. Cellos, bad and good, are particularly prone to this problem.

In previous work, a computational method that allows efficient time-domain modelling of bowed strings based on a modal approach has been introduced. This has been extended to incorporate the complex dynamics of real-life instrument bodies, and their coupling to the string motions, using experimental dynamical body data. The string is modelled using its unconstrained modes, assuming pinned–pinned boundary conditions at the tailpiece and the nut. At the intermediary bridge location, the string–body coupling is enforced using the body impulse-response or modal data, as measured at the instrument bridge.

In the present paper, this computational approach is applied to a specific cello, which provided experimental wolf-behaviour data under several bowing conditions, as well as laboratory measurements of the bridge impulse responses on which the numerical simulations were based. Interesting aspects of the string–body dynamical responses are highlighted by numerical simulations and the corresponding sounds and animations produced. Finally, a qualitative (and, when possible, quantitative) comparison of the experimental and numerical results is presented.

1. Introduction

Raman's seminal paper [1] was a landmark study of the dynamics of bowed strings. Since then, a plethora of research papers has been published on bowed-string instruments, including enlightening work by Friedlander [2], Schelleng [3], McIntyre et al. [4], to name just a few (see Cremer's book [5], for an extensive account of the field).

*Corresponding author. Tel.: +351 912598121; fax: +351 1229480322.
E-mail address: OctavioInacio@esmae-ipp.pt (O. Inácio).

0022-460X/$ - see front matter © 2007 Elsevier Ltd. All rights reserved.
doi:10.1016/j.jsv.2007.07.079

Nomenclature

Variables

a	number of bow hairs assumed in contact with the string
A	cross-sectional area of a bow hair
b	number of modelled bow hairs
B	inharmonicity parameter
c	wave speed in string
$\mathbf{C}$	modal damping matrix
C	friction decay parameter
C_a	lumped adherence damping of the total modelled bow hairs
$\bar{C}_a$	adherence damping of a single bow hair
C_{bs}	bridge–string damping coupling coefficient
E	Young's modulus
F	force
$\mathbf{F}$	modal force matrix
$\Im_n(t)$	modal force
h	bridge impulse response
H	length of the bow hair
i	time step index
J_i	product of contact point velocities at successive time steps
$\mathbf{K}$	modal stiffness matrix
K_B	body parameter
K_{bs}	bridge–string stiffness coupling coefficient
K_a	lumped adherence stiffness of the total modelled bow hairs
$\bar{K}_a$	adherence stiffness of a single bow hair
L	length of string
$m_a{}^B$	body parameter
m_n	modal mass
$\mathbf{M}$	modal mass matrix
n	mode number
N	maximum n
q_n	modal response
$\mathbf{Q}$	modal response matrix
S	cross-sectional area of string
t	time
T	tension
x	axial position
y	transverse displacement
ζ_n	modal damping
η	dissipation coefficient
μ	friction coefficient
ρ	density
φ_n	modeshape
ω_n	circular eigenfrequency

Subscripts

A, a	adherence
$a1$	related to the left side of the bow hair in relation to the contact point
$a2$	related to the right side of the bow hair in relation to the contact point
b	bridge
B	body
bow	bow
bs	bridge–string
c	contact point
d	dynamic
D	asymptotic dynamic
f	frictional
N	normal
s	slip
S	static

Although modal methods have been extensively used in more general and specific industry-related problems [6,7], its use in simulation of musical instruments behaviour is far from widespread. In previous work, a modal method was developed to deal with plucked and bowed strings [8–11], enabling an effective simulation of such systems, even when dispersive effects are significant. As in much other published work, those simulations assumed a string pinned at the bridge and the nut, and therefore decoupled from the instrument body. This approach proved adequate to obtain the typical motion patterns displayed by bowed strings. However, because the bridge is assumed motionless, such computations are obviously unable to cope with more subtle phenomena related to the coupling of string and body motions.

A crude approach to incorporate body effects, when simulating string sounds, is to start by computing the vibratory response of an "isolated" (bowed or plucked) string, and then use the resulting string–bridge interaction force to drive a given body vibro-acoustic transfer function. However, this simple approach is quite limited and cannot account for any energy feedback from the body into the string—such as is found in wolf notes—because the full string–body coupling is not modelled.

Apparently, only a few authors have attempted to address this string–body coupling problem. McIntyre et al. [4] incorporated in their wave-propagation computational algorithm a bridge-reflection function which encapsulates the dynamical behaviour of a given body resonance, enabling them to simulate the coupled dynamics between the string and the chosen body resonance. Similarly, Puaud et al. [12] used (in connection with a so-called "numerical bow") a mass-stiffness bridge resonator, therefore also emulate a chosen body-resonance coupled to the string dynamics. Recently, a different approach has been pursued by several authors to simulate instrument bodies and cavities (see Huang et al. [13], for instance) by using 2D or 3D waveguides to compute simplified multi-degree-of-freedom resonating systems. However, until now, this modelling technique has only been used to simulate the body-filtering effects on string–bridge dynamical forces, with no feedback coupling. In relation to other stringed instruments, Derveaux et al. [14] achieved fully coupled string/soundboard computations for a modelled guitar.

The aim of the present work is to simulate the interaction between strings and real-life instrument bodies, where our computational method is extended to incorporate the multi-modal dynamics of a violin and cello body, fully coupled to the string motions. A hybrid approach is taken, in the sense that a theoretical model of the string is coupled with dynamical body data, obtained either from simplified models or real-life experiments.

The string is modelled using its unconstrained modes assuming in contrast with [8–11], pinned–pinned boundary conditions at the tailpiece and the nut. Then, at the bridge location, the string–body coupling is enforced using the body impulse-response or modal data (as measured at the bridge). At each time step, the system motion is computed by integrating the string-modal equations, excited by the modally projected values of the frictional bow force and also of the string–bridge contact force. The latter is obtained from the body motion at each time-step, as computed either (a) using the body impulse response, or (b) from a modal model of the body. In the first method, the body dynamics are obtained through incremental convolution, a costly procedure which, however, enables the direct simulation of real bodies without any further modelling assumptions or simplifications. The second method allows for faster computations, but demands a computed or identified modal model of the instrument body.

It should be mentioned here that the modal basis unconstrained at the bridge location (coupling point) is not the only option available to solve this problem. Indeed the interested reader may refer to the recent work by Woodhouse [15], who deals with body–string coupling in guitars by modelling the string as pinned–pinned at the nut and the bridge, and then complements such basis with a so-called "constraint mode" which can be shown to be the static response of the string when the bridge extremity is moved [16]. Similar issues arise when dealing with sub-structure synthesis where the analyst may choose between several families of the basis functions used to represent each substructure (refer, for instance to Ref. [6]). The merits of the various approaches will be reflected on the number of basis terms used to achieve convergence. However, a comparison of these different methods is beyond the scope of this paper.

After a few demonstrative experiments and a detailed presentation, our computational approaches are illustrated for both violin and cello typical self-excited string motion regimes. These are compared for "isolated" strings and for the string–body coupled model, based here on synthetic body dynamical data. In particular, interesting simulations pertaining to the so-called wolf notes are presented.

2. Computational method

2.1. Formulation of the string dynamics

Consider an ideal string of length L and cross-sectional area S, linear density ρS and dissipation coefficient η, subject to a constant axial tensile force T and a force distribution $F(x,t)$. The small-amplitude transverse motion $y(x,t)$ of the string is basically described by the wave-equation [6]:

$$\rho S \frac{\partial^2 y}{\partial^2 t} = T \frac{\partial^2 y}{\partial x^2} + F(x,t), \tag{1}$$

where the wave speed is given by $c^2 = T/(\rho S)$. In practice, physics imposes that Eq. (1) embeds some kind of damping effect in order to cope with the actual behaviour of the various dissipative mechanisms acting on the

string (string radiation, internal damping) [17]. However, we will assume here, for simplicity, that the damping mechanism leads to proportional damping on the string and, therefore, to real modes.

Any solution of a suitable damped version of Eq. (1) can be formulated in terms of the string's modal parameters: for modeshapes normalised at unitary maximum values modal masses are given as $m_n = \rho SL/2$ ($\forall n$). Other modal parameters are the circular frequencies $\omega_n = n\pi c/L$, damping values ζ_n and mode shapes $\varphi_n(x) = \sin(n\pi x/L)$, with $n = 1, 2, \ldots, N$. The order N of modal truncation is problem dependent and must be asserted by physical reasoning. On the modal space the forced response of the damped string is formulated by Eq. (2), which follows from Eq. (1) by writing the solution of this partial-differential equation with the separation approach (4):

$$[\mathbf{M}]\{\ddot{\mathbf{Q}}(t)\} + [\mathbf{C}]\{\dot{\mathbf{Q}}(t)\} + [\mathbf{K}]\{\mathbf{Q}(t)\} = \{\mathbf{F}(t)\}, \tag{2}$$

where $[\mathbf{M}] = \mathrm{diag}(m_1, \ldots, m_N), [\mathbf{C}] = \mathrm{diag}(2\, m_1\omega_1\, \zeta_1, \ldots, 2\, m_N\omega_N\, \zeta_N), [\mathbf{K}] = \mathrm{diag}(m_1\omega_1^2, \ldots, m_N\omega_N^2)$, are the matrices of modal parameters, $\{\mathbf{Q}(t)\} = \langle q_1(t), \ldots, q_N(t)\rangle^{\mathrm{T}}$ and $\{\mathbf{F}(t)\} = \langle \Im_1(t), \ldots, \Im_N(t)\rangle^{\mathrm{T}}$ are the vectors of modal responses and generalised forces, respectively. The damping values ζ_n are usually identified from experiments. However, they could, where appropriate, be theoretically modelled [17]. The modal forces $\Im_n(t)$ are obtained by projecting the external force field on the modal basis:

$$\Im_n(t) = \int_0^L F(x,t)\varphi_n(x)\mathrm{d}x \quad (n = 1, 2, \ldots, N). \tag{3}$$

The physical motions at any point of the string can be computed from the modal amplitudes $q_n(t)$ by superposition:

$$y(x,t) = \sum_{n=1}^{N} \varphi_n(x)\, q_n(t) \tag{4}$$

and similarly concerning the velocities and accelerations. For given external excitation and initial conditions, the previous system of equations can be integrated using an adequate time-step integration algorithm. Explicit integration methods are well suited for the friction model used here. In our implementation, we used the so-called Velocity–Verlet integration algorithm [18], which is a low-order explicit scheme (see Section 2.4). Note that although (2–4) obviously pertain to a linear formulation, nothing prevents us from including in $\Im_n(t)$ all nonlinear effects arising in the system. Accordingly, the system modes become coupled by the nonlinear effects.

For the present case, the external force field $F(x,t)$ is due to the excitation friction force $F_{s,a}(x_c,t)$ provided by the bow (which we will model in this paper as a single hair bow, although we can easily introduce excitation by a bow of finite width—see Ref. [11]), by the interaction force $F_b(x_b,t)$ between the body and the string at the bridge and by the possible presence of a finger on the fingerboard (see Fig. 1).

2.1.1. Friction model

Friction-related phenomena have been subject of a considerable amount of research, and several models have emerged to address a number of related problems. Due to the complexity of the interaction between contacting surfaces and of the associated high nonlinearity, most models are of an empirical nature. A survey of the experimental and analytical knowledge in this field can be found in Refs. [19–24].

The friction model used in this work is based on ideas proposed by Antunes et al. [25] in the context of an industrial vibro-impact problem, using at that time, velocity-independent sliding friction coefficient. In the

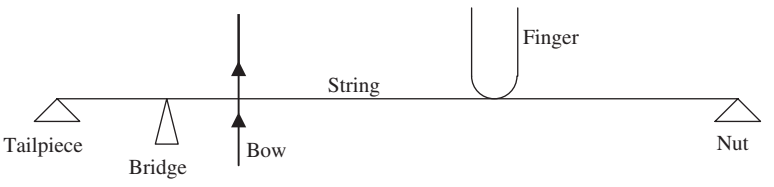

Fig. 1. Idealised model of the bowed string.

present paper, adherence is modelled using the concept of spring/damping attachment point, while sliding is modelled by fitting an empirical formulation to experimental published data [26].

The friction force arising between the string and the bow hair at location x_c of the string is given by

$$\begin{cases} F_s(x_c,t) = -\mu_d(\dot{y}_c)\dfrac{F_N}{b}\mathrm{sgn}(\dot{y}_c), & \text{if } |\dot{y}_c| > 0, \\ |F_a(x_c,t)| < \mu_S\dfrac{F_N}{b}, & \text{if } |\dot{y}_c| = 0, \end{cases} \tag{5}$$

where F_N is the normal force between the bow and the string, μ_S is a "static" friction coefficient (used during surface adherence), $\mu_d(\dot{y}_c)$ is a "dynamic" friction coefficient (used for sliding regimes) and b is the number of bow hairs used in the model. This friction model is depicted in Fig. 2. Here, the relative transverse velocity between the bow and the string is given by

$$\dot{y}_c(t) = \dot{y}(x_c,t) - \dot{y}_{\mathrm{bow}}(t) = \sum_{n=1}^{N} \varphi_n(x_c)\dot{q}_n(t) - \dot{y}_{\mathrm{bow}}(t). \tag{6}$$

In this work we assume that $\mu_d(\dot{y}_c)$ is a function of the relative bow–string velocity, and use the following model:

$$\mu_d(\dot{y}_c) = \mu_D + (\mu_S - \mu_D)\mathrm{e}^{-C|\dot{y}_c|}, \tag{7}$$

where $0 \leqslant \mu_D \leqslant \mu_S$ is an asymptotic lower limit of the friction coefficient when $|\dot{y}_c| \to \infty$, and parameter C controls the decay rate of the friction coefficient with the relative bow–string sliding velocity. The friction model (7) can be readily fitted to typical experimental data, by adjusting the empirical constants μ_S, μ_D and C.

The sliding behaviour, described by the first relation in Eq. (5), does not cause problems for simulations, as this equation explicitly shows how the sliding force should be computed as a function of the sliding velocity. However, during adherence, simulation becomes more difficult. Indeed, the second equation in Eq. (5) merely states a limiting value for the friction force, during adherence, and gives no hint on how $F_a(\dot{y}_c,t)$ may be actually computed. This is because the adherence force depends on the overall balance of all internal and external forces acting upon the system, which are quite complex for multi-degree-of-freedom problems. Although the Friedlander construct [2] used by many investigators in this field leads to very fast computations of the responses at the bowing point, many friction algorithms deal with this problem through costly iterative

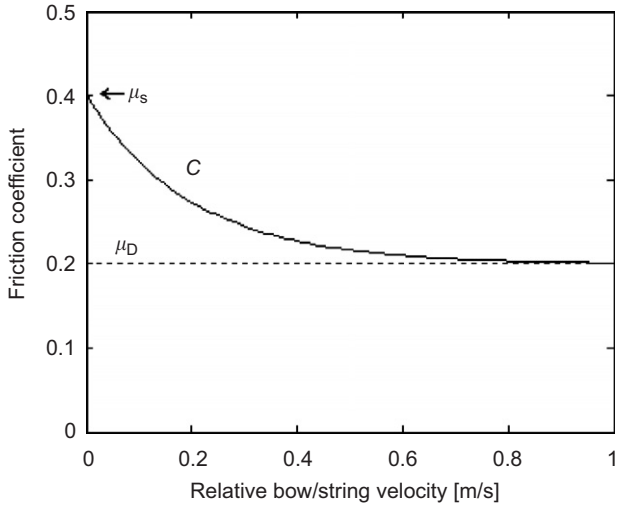

Fig. 2. Change of the friction coefficient with the bow–string relative velocity.

numerical schemes, which may be quite expensive to run. In our approach, the following explicit procedure is used at each time-step i:

(1) If in the previous time-step the system was sliding, we start by detecting a possible bow-hair–string adherence, by computing $J_i = \dot{y}_c(t_i)\dot{y}_c(t_{i-1})$. Then, if $J_i > 0$, the system is still sliding in the same direction. We compute $F_s(\dot{y}_c, t_i)$ according to the first relation in Eq. (5), with $\dot{y}_c(t_i)$ given by Eq. (6) and $\mu_d(t_i)$ by Eq. (7).

(2) However, if $J_i \leqslant 0$, then a reversal of the relative motion is occurring and adherence will arise. Then, we compute the sticking force using the following model:

$$F_a(x_c, t_i) = -K_a y_c(t_i) - C_a \dot{y}_c(t_i), \tag{8}$$

which will be used during the complete duration of the adherence state. The idea in Eq. (8) is to "attach" the string to the bow at point x_c using a suitable "adherence stiffness" and to damp-out any residual bow/string relative motion during sticking using an "adherence damping" term in Eq. (8). y_c is the relative displacement between the string and the bow hair, at any time during adherence, given as:

$$y_c = y(x_c, t) - y^a_{\text{bow}}(t) = \sum_{n=1}^{N} \varphi_n(x_c)\, q_n(t) - y^a_{\text{bow}}(t) \tag{9}$$

where $y^a_{\text{bow}}(t)$ is the current position of the bow contact point. For a given constant bow speed, this changes as $y^a_{\text{bow}}(t) = (t - t_a)\ \dot{y}_{\text{bow}}$, where t_a is the time value when adherence was detected. The adherence stiffness K_a in Eq. (8) is computed from

$$\bar{K}_a = \bar{K}_{a1} + \bar{K}_{a2}, \tag{10}$$

where $\bar{K}_{a1}$ and $\bar{K}_{a2}$ are related to the axial stiffness of the bow hair on each side of the contact point. Although the real axial stiffness will change as the contact point moves along the bow, $\bar{K}_{a1}$ and $\bar{K}_{a2}$ are here assumed for simplicity to be equal and given by

$$\bar{K}_{a1} = \bar{K}_{a2} = \frac{EA}{H/2} \tag{11}$$

which would pertain to a bow acting about its middle length. Any correction to this assumption can be easily established in this model. In Eq. (11) E is the Young Modulus, A the cross-section of one individual bow hair and H the total length of the bow hair. The adherence stiffness of each contact point is given by

$$K_a = \bar{K}_a a/b, \tag{12}$$

where a is the number of bow hairs assumed in contact with the string, and b is the number of pseudo-bow hairs (contact points) used in the numerical model. Similarly, $C_a = \bar{C}_a a/b$, where $\bar{C}_a$ is the adherence damping of a single bow hair.

(3) After computing the adherence force, $F_c(\dot{y}_c, t_i)$ is compared with the maximum allowable value $\mu_S F_N$. If $|F_a| \leqslant \mu_S F_N$, the current estimate is accepted and simulation continues assuming a sticking state. On the contrary, when $|F_a| > \mu_S F_N$, sliding will arise and the friction force is recomputed according to the first relation in Eq. (5). Then, the procedure continues with the next time-step. Again, we stress that, by virtue of (6) and (9), all the string modes become coupled when the nonlinear friction force is projected on the modal basis, Eq. (3), and then incorporated in Eq. (2).

In this context, it should be mentioned that recent research results [27] suggest the relevance of dynamical thermal phenomena in the tribology of rosin, which may induce hysteretic effects in the friction-velocity dependence. In spite of the unquestionable interest of such findings, the classical approach for sliding behaviour was used, as this article addresses a different issue.

2.2. Formulation of the body dynamics

As previously explained, the present method was implemented to simulate the influence of the string–body coupling using two different procedures: incremental convolution of a measured impulse response or through a modal model of the body dynamics.

2.2.1. Incremental convolution formulation

At the bridge, the string motion forces the violin body into vibration. The response of the body can be computed, at each time step i, by the incremental convolution of the time-history of the interaction force between the bridge and the string $F_b(x_b,t)$ and the body impulse response function $h_b(t)$ at the same point x_b, according to Eq. (13):

$$y_b(x_b,t) = \int_0^t F_b(x_b,\tau)h_b(t-\tau)\mathrm{d}\tau, \tag{13}$$

where $y_b(x_b,t)$ is the displacement of the bridge at the contact point with the string, while $h_b(t)$ is the displacement/force impulse-response functions of the instrument body, measured at the bridge, along the horizontal direction (see Fig. 4).

2.2.2. Modal formulation

As for the string, we will assume that in the instrument body damping is proportional and hence body modes are also real. This assumption is debatable, as discussed in Ref. [15], but will be adopted here to avoid the additional burden of using a complex modal basis. Notice, however, that if the direct convolution formulation (13) is used, the possible complexity of body modes is already embedded in the body impulse response $h_b(t)$ and introduces no further difficulty. The response of the body of the instrument can be represented by a simplified modal model:

$$[\mathbf{M}_B]\{\ddot{\mathbf{Q}}_B(t)\} + [\mathbf{C}_B]\{\dot{\mathbf{Q}}_B(t)\} + [\mathbf{K}_B]\{\mathbf{Q}_B(t)\} = \{\mathbf{F}_B(t)\}, \tag{14}$$

where $[\mathbf{M}_B] = \mathrm{diag}(m_1^B,\ldots,m_P^B), [\mathbf{C}_B] = \mathrm{diag}(2\,m_1^B\omega_1^B\,\zeta_1^B,\ldots,2\,m_P^B\omega_P^B\,\zeta_P^B), [\mathbf{K}_B] = \mathrm{diag}(m_1^B(\omega_1^B)^2,\ldots,m_P(\omega_P^B)^2)$, are the matrices of the body modal parameters, $\{\mathbf{Q}_B(t)\} = \langle q_1^B(t),\ldots,q_P^B(t)\rangle^{\mathrm{T}}$ and $\{\mathbf{F}_B(t)\} = \langle \Im_1^B(t),\ldots,\Im_P^B(t)\rangle^{\mathrm{T}}$ are the vectors of modal responses and generalized forces, respectively. The modal forces $\Im_p^B(t)$ are obtained by projecting the string–body coupling force $F_b(x_b,t)$ (see Section 2.3), on the body modal basis. The modal parameters are identified from a single transfer function measurement at the bridge, $H_b(\omega) = \mathsf{F}[h_b(t)]$, where F denotes the Fourier transformation. This fact leads to a requirement that the modal mass matrix should be normalised by postulating that all modeshapes $\varphi_p^B(x_b)$ are unitary at the bridge location. The physical motions at the bridge are then computed from the modal amplitudes $q_p^B(t)$ by superposition:

$$y_b(x_b,t) = \sum_{p=1}^{P} q_p^B(t). \tag{15}$$

2.2.3. Discussion of the body dynamics formulation methods

Both methods described before have advantages and disadvantages from the computational point of view. The incremental convolution method allows the use of measured impulse response functions of real-life instruments, without any other assumptions other than linearity, nor does it require the use of any modal identification procedure. It allows the most accurate representation of the body dynamics, but has the great disadvantage of requiring long-computation times if the direct convolution formulation (13) is used. This problem can, however, be alleviated by the implementation of some form of fast-convolution approach. On the other hand, the modal approach of the body allows for much lower computation times (at least by one order of magnitude), but requires a careful modal identification to be performed. Furthermore, the modal representation is less than ideal to cope with the body dynamics at higher-frequency modal densities because of the large number of modes that would be required. Computation times are proportional to the number of modes used in the model. In contrast, the incremental convolution procedure's computation time does not depend on the modal order but only on the duration of the impulse-response function. Finally, it should be emphasised that although not presented in this paper, vertical motion of the string and bridge can be easily implemented with this computational method.

2.3. Formulation of the string–body coupling

The coupling between the string and the body of the violin arises from the bridge–string contact force $F_b(x_b,t)$ which is used in Eqs. (2), (13) and (14). In this paper we model this interaction by connecting the string to the bridge through a very stiff spring and a dashpot to prevent parasitic oscillations:

$$F_b(x_b,t) = K_{bs}[y_b(x_b,t) - y_s(x_b,t)] + C_{bs}[\dot{y}_b(x_b,t) - \dot{y}_s(x_b,t)], \tag{16}$$

where K_{bs} is the stiffness coupling coefficient between the bridge and the string, C_{bs} is the damping coupling coefficient between the bridge and the string and $y_s(x_b,t)$ and $y_s(x_b,t)$ are the displacement and velocity of the string at the bridge, respectively.

2.4. Integration algorithm

The modal Eqs. (2) and (14), coupled through the right-hand side force terms, may be numerically integrated using either an explicit or implicit approach, meaning that the dynamical force balance may be based on the state of the system at either the last computed time-step t_i or the next time-step $t_{i+1} = t_i + \Delta t$ under computation. Both approaches have merits and disadvantages as, in broad terms, explicit algorithms are simpler and faster per time-step than implicit algorithms, which must iterate until convergence. However, the latter typically enable the use of larger integration time-steps Δt, which may compensate the previous disadvantage, the best option being problem dependent. Previous experience with vibro-impacting and friction-excited systems (see Refs. [8–11,28]) suggests that explicit algorithms are well suited for such problems. Among other possible choices the so-called ''Velocity-Verlet'' method introduced in Ref. [29] is used here. This is a simple explicit algorithm of second order. Although not frequently found in structural dynamics computations, this algorithm has been widely used by researchers dealing with granular flow and molecular dynamics computations—see Ref. [30], for instance. However, other methods such as Newmark's algorithm [31,32] might be used as well.

Please notice that because numerical efficiency is not an issue here, it is not claimed that the time-step integration algorithm used in the paper is the most efficient approach for the problem.

For each modal equation, the Velocity–Verlet algorithm is expressed as

$$\begin{aligned} q_n(t_{i+1}) &= q_n(t_i) + \dot{q}_n(t_i)\triangle t + \frac{\triangle t^2}{2}\frac{\Im_n(t_i)}{m_n} + O(\triangle t^3), \\ \dot{q}_n(t_{i+1}) &= \dot{q}_n(t_i) + \frac{\triangle t}{2}\frac{\Im_n(t_i) + \Im_n(t_{i+1})}{m_n} + O(\triangle t^3), \end{aligned} \tag{17}$$

where, because the interaction forces depend on the system response, we have $\Im_n(t_i) = \Im_n[q_j(t_i),\ \dot{q}_j(t_i)]$ and, strictly speaking, $\Im_n(t_{i+1}) = \Im_n[q_j(t_{i+1}),\ \dot{q}_j(t_{i+1})]$ (where the index j stands for all modes in the range $j = 1,\ldots,N$). However, the use of such expression for $\Im_n(t_{i+1})$ would enforce an implicit scheme. In practice, formulation (1) may be split as follows:

$$\begin{aligned} \dot{q}_n(t_{i+1/2}) &= \dot{q}_n(t_i) + \frac{\triangle t}{2}\frac{\Im_n(t_i)}{m_n}, \\ q_n(t_{i+1}) &= q_n(t_i) + \dot{q}_n(t_{i+1/2})\triangle t, \\ \dot{q}_n(t_{i+1}) &= \dot{q}_n(t_{i+1/2}) + \frac{\triangle t}{2}\frac{\tilde{\Im}_n(t_{i+1})}{m_n}, \end{aligned} \tag{18}$$

with $\Im_n(t_i) = \Im_n[q_j(t_i), \dot{q}_j(t_i)]$ and the approximation $\tilde{\Im}_n(t_{i+1}) \cong \Im_n[q_j(t_{i+1}), \dot{q}_j(t_{i+1/2})]$ is used instead of the unknown value $\Im_n(t_{i+1})$.

3. The wolf note

The wolf note is a particular effect to which bowed-string instruments (bad or good) are known to be very susceptible. It is an unpopular phenomenon among musicians since it gives rise to harsh and beating-like

sounds, making proper musical execution extremely difficult at some positions along the fingerboard. Although unpleasant for the listener, the emergence of this effect is paradigmatic of the importance of the body–string interaction.

The wolf phenomenon has been the subject of several studies [1,12,33–38], the most generally accepted explanation being the one suggested by Schelleng [33], 40 years ago. More recently the basis of this explanation has been revisited and further discussed by Woodhouse [38]. However, there are still a few aspects deserving exploration, such as the influence of the string dynamics in the portion between the tailpiece and the bridge (see Ref. [14] for an interesting experimental account). On the other hand, we experienced a dependence of the wolf-beating frequency on the bowing parameters, an aspect which seems almost absent from the literature, other than in Ref. [4] where two simulations of a wolf note played with different bow forces are shown, exhibiting different wolf-beating frequencies. Also, the emergence of wolf phenomena appears to depend somewhat on the time-history of the bowing parameters, a fact which has also been noted in Ref. [14]. These issues will be addressed in the present and future papers.

3.1. Wolf note measurements

In order to explore the coupling between the body of the instrument and the strings, some preliminary measurements were made on a cello. Fig. 3 shows a typical mobility frequency response function measured at the bridge in the horizontal direction as shown in Fig. 4, through impact excitation, the bridge response being sensed by an accelerometer. After careful consideration it was decided to, similar to Ref. [15], perform the measurements keeping the strings of the instrument tensioned and in-tune but damped with a light cloth.

The main body resonance occurs at approximately 196 Hz with a relatively low damping ratio ($\zeta = 0.7\%$) when compared with the majority of the other peaks which reveal damping ratios of the order of 2%. This high amplitude mobility peak ($1.63 \times 10^{-1}\,\mathrm{m\,s^{-1}\,N^{-1}}$) is responsible for the wolf note.

Figs. 5–7 show several typical time-histories, and corresponding spectra, to excitation by bowing on the C_2 open string (tuned to 65.4 Hz) at different notes on the fingerboard. Typical velocity amplitudes for the vibration of the bridge at the C_2 open string are shown to be of the order of 0.1–0.2 $\mathrm{m\,s^{-1}}$. At a bowing position of approximately 40 mm from the bridge (Fig. 5), the third harmonic is prevalent relative to the lower order partials. The proximity of its frequency to the main body resonance ($3 \times 65.4\,\mathrm{Hz} = 196.2\,\mathrm{Hz}$) enhances this particular harmonic, revealing the importance of string–body coupling for normal musical regimes.

Fig. 6 depicts the typical amplitude-modulated waveform that characterizes the wolf note. In order to achieve this sound, the C_2 string was stopped at a distance approximately $L/3$ from the bridge (where L is the length of the string), and the G_3 note was played at approximately 196 Hz. Clearly, the beating phenomena displayed is the result of strong coupling between the string vibration and the main body resonance, which is

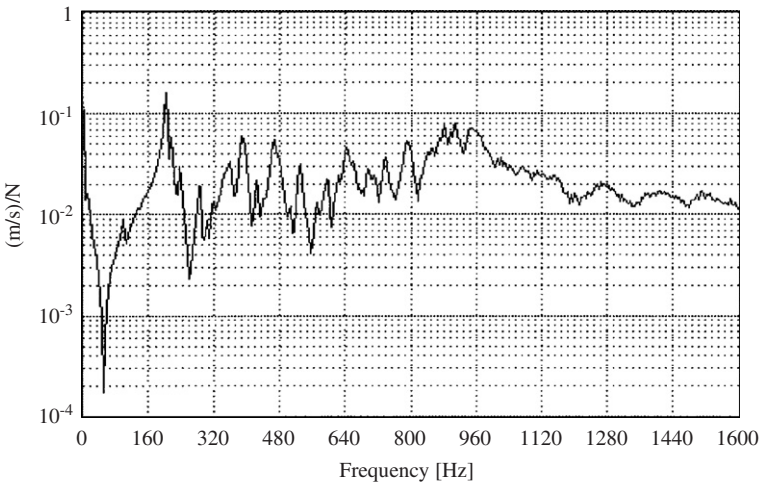

Fig. 3. Mobility transfer function of the cello measured at the bridge.

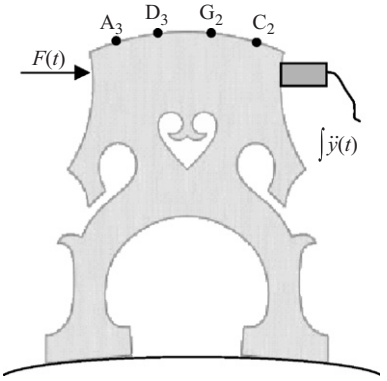

Fig. 4. Set-up used for the transfer function measurements.

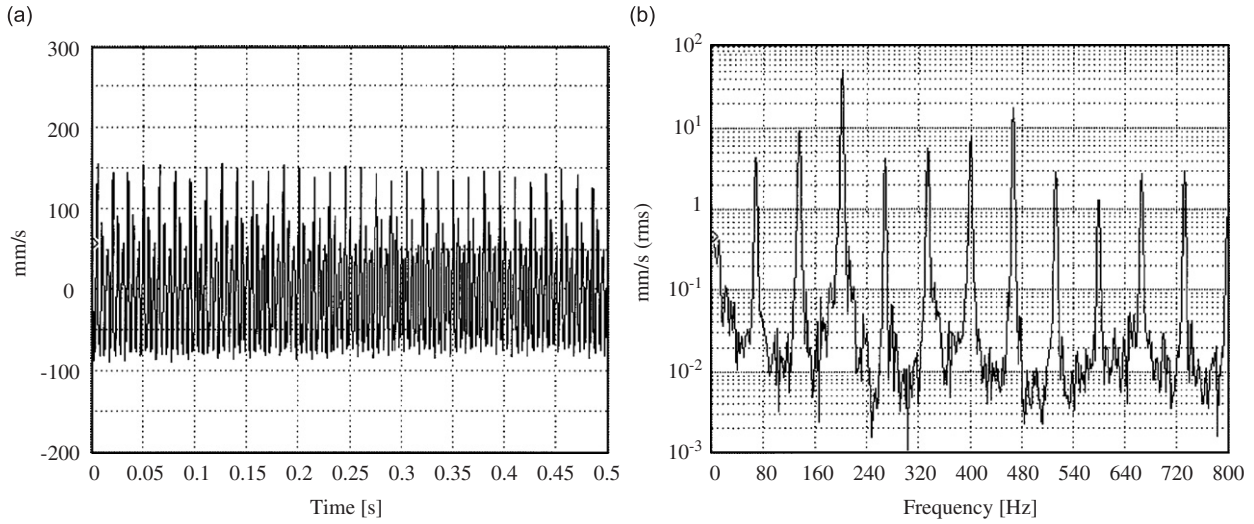

Fig. 5. Velocity time-history and spectrum of the bridge vibration, resulting from bowing on the C_2-open string.

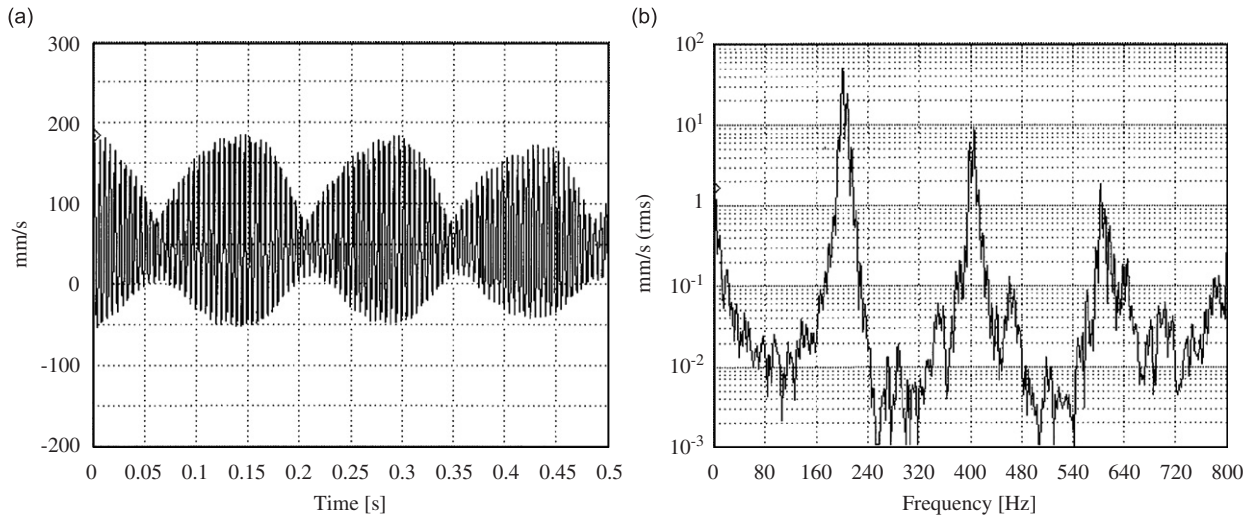

Fig. 6. Velocity time-history and spectrum of the bridge vibration, resulting from bowing on the C_2 string at a fingerboard position approximately $L/3$ from the bridge (generating here a wolf note).

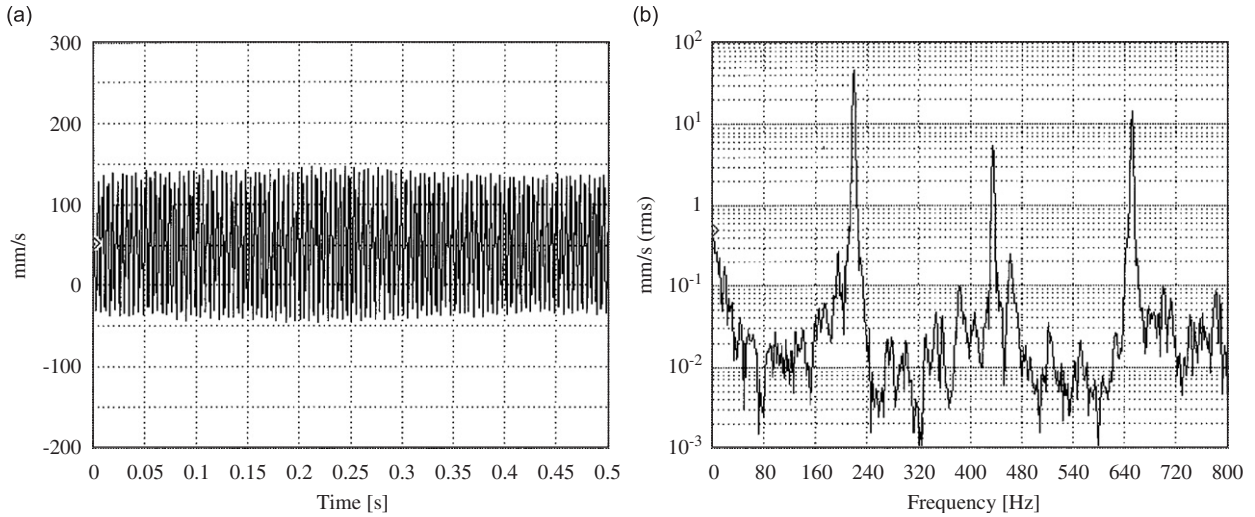

Fig. 7. Velocity time-history and spectrum of the bridge vibration, resulting from bowing on the C_2 string at a fingerboard position about one semitone above the wolf note (compare with Fig. 5).

related to the proximity of their frequencies. Shortening the effective length of the string by a small amount is enough to prevent the wolf note to develop as can be seen in Fig. 7. In this case, the finger moved along the fingerboard in the direction of the bridge a few millimetres, which was enough to alter the fundamental frequency of the stopped string to 218 Hz which prevented the strong string–body coupled response.

4. Simulations

Simulations were performed for both a violin and a cello. The movement of a violin G-string with a fundamental frequency of 196 Hz is simulated, with an effective length $L = 0.33\,\mathrm{m}$ and a linear density of $\rho S = 3.1 \times 10^{-3}\,\mathrm{kg\,m^{-1}}$, in order to test the behaviour of the coupled computation method described above. The cello C-string simulated has a total length of 0.83 m from the nut to the tailpiece with 0.7 m and a linear density of $\rho S = 14 \times 10^{-3}\,\mathrm{kg\,m^{-1}}$ from the bridge to the nut, giving a fundamental frequency of 65.4 Hz. In order to achieve adequate computational convergence 60 modes were used for the violin string and 80 modes for the cello string, with a recorded sampling frequency of 20 000 Hz. For simplicity, a modal damping value of 0.1% was used for all modes (however, frequency-dependent damping can be easily introduced with this method) and a string inharmonicity coefficient B was introduced to provide more realistic simulations [3,5]. This effect is easily simulated using our approach, as the bending stiffness influence is automatically incorporated in the string modes, with modified frequencies according to

$$\omega_n = n\omega_1\sqrt{1 + Bn^2}, \quad \text{for } n \geqslant 2, \tag{19}$$

where $B = \pi E\phi^4/64L^2T$ for homogeneous strings. However, the lower strings for the violin or cello are usually wound and therefore nonhomogeneous, so a value of $B = 2.33 \times 10^{-4}$ was used, which was inferred from Table 4.9 of Ref. [39].

The bodies of the violin and the cello were simulated using a modal basis whose parameters were identified from measured input admittances. In the case of the violin a very crude model was used comprising only 13 modes covering the frequency range between 200 and 3500 Hz. In the case of the cello a thorough modal-identification procedure was carried and 53 modes were chosen leading to the synthesised input admittance shown in Fig. 8.

A classic sliding law friction model, such as the one presented in Eq. (7), with $\mu_S = 0.4$, $\mu_D = 0.2$ and $C = 5$, was chosen, which produced realistic results. For the adherence model a total value of $K_a = 10^5\,\mathrm{N\,m^{-1}}$ has

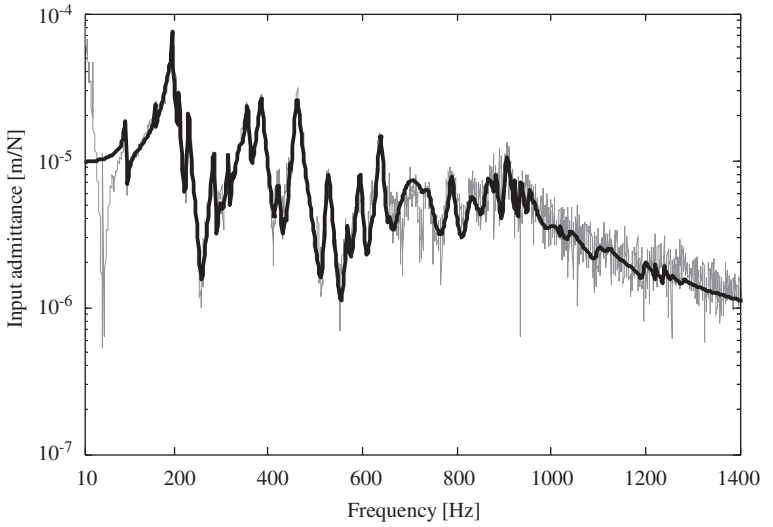

Fig. 8. Measured (light line) and synthesised (heavy line) input admittance of the cello used in the simulations.

been used. As previously discussed, a near-critical value of the adherence damping term C_a was adopted [10,11].

The stiffness constant value, K_{bs}, used for the string–body coupling was chosen in order to enable a very stiff connection, while keeping a satisfactory computational convergence. As demonstrated in Appendix A a value equal or higher than $10^6\,\mathrm{N\,m^{-1}}$ is enough. Concerning the damping constant a value $C_{bs} = 10\,\mathrm{Ns\,m^{-1}}$ proved adequate. As also shown in Appendix A, for $K_{bs} \geqslant 10^6\,\mathrm{N\,m^{-1}}$ the modal damping of the string–body coupled modes is not affected by this value of C_{bs}.

5. Results

5.1. Violin simulation results

Figs. 9–11 show simulations of the violin string and bridge dynamics for different boundary conditions, when applying a normal bow force (F_N) of 1 N and bow velocity ($\dot{y}_{\mathrm{bow}}$) of $0.1\,\mathrm{m\,s^{-1}}$, at 0.030 m (approximately $L/10$) from the bridge. Fig. 9 shows the most widely simulated case of a string pinned at the bridge and the nut (with a length of 0.330 m). Perfect reflections arise from these extremities and the Helmholtz motion is clearly perceptible. The force at the bridge is easily computed from the modal time responses $q_n(t)$, through a superposition of the modal reaction forces, Eq. (20), where f_1 is the fundamental frequency of the string:

$$F_b(t) = -4\pi\frac{\rho}{S}Lf_1^2\sum_{n=1}^{N} nq_n(t). \tag{20}$$

Fig. 10 represents the case of a string pinned at the tailpiece and the nut, with a total length of 0.385 m, a rigid bridge being placed at 0.330 m from the nut. The same overall behaviour as in the previous example could be expected, since there is no movement of the bridge. However, note that the string inharmonicity enables some energy to pass to the tailpiece side of the string, leading to low-amplitude waves at higher frequency. These parasitic oscillations are clearly perceptible in the string–bridge coupling force shown in Fig. 10, superimposed on the well-known bow-bridge secondary waves shown in Fig. 9. This effect, noted by Puaud et al. [12], can be seen very clearly on the computed animations of the string motion. Nevertheless, and not unexpectedly, a Helmholtz motion similar to the previous example developed. Notice that the overall behaviour of the string-bridge contact force is similar for the computations in Figs. 9 and 10. This is a

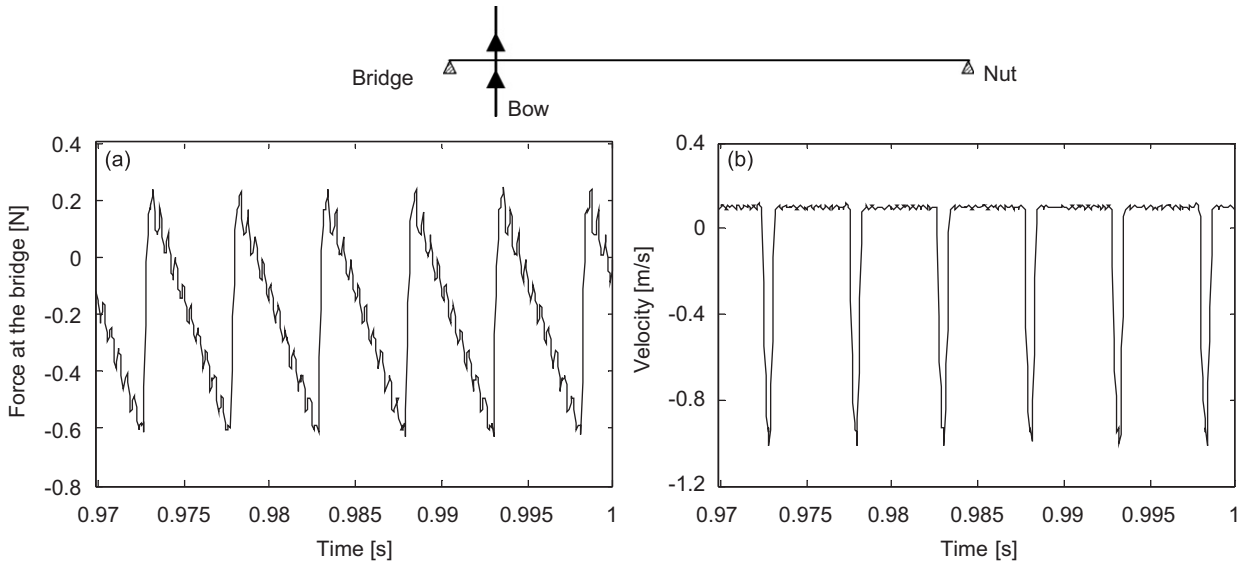

Fig. 9. Force at the bridge and string velocity at the bow contact point for a 0.330 m string pinned at both extremities ($F_N = 1$ N, $\dot{y}_{\text{bow}} = 0.1$ m s^{-1}).

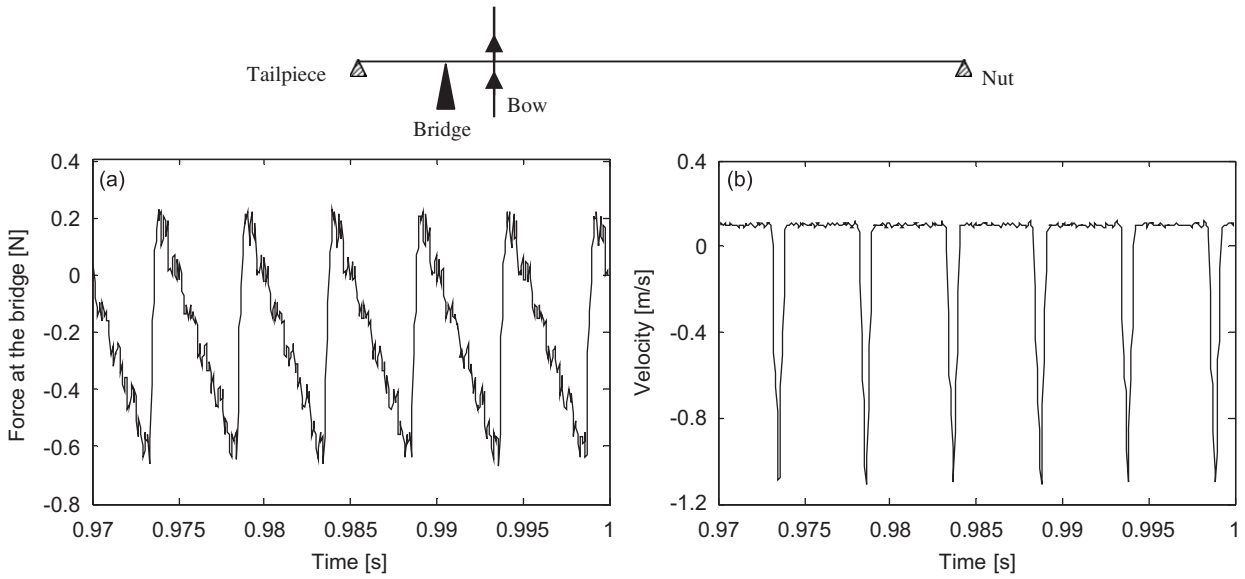

Fig. 10. Force at the bridge and string velocity at the bow contact point for a 0.385 m string pinned at the nut and tailpiece (rigidly supported bridge at 0.330 m, $F_N = 1$ N, $\dot{y}_{\text{bow}} = 0.1$ m s^{-1}).

reassuring feature, given that in Fig. 9 the contact force is computed from the modal summation of Eq. (20), while in Fig. 10 the interaction force stems from the totally different approach stated in Eq. (16).

Fig. 11 shows the results obtained from the simulations computed through the implementation of the string–body coupling by application of the modal model of a violin body (Section 2.2.2). A modal identification was performed, as pointed before, on a mass-produced violin and 13 modes were chosen to represent the gross features of its dynamical behaviour. The corresponding synthesised impulse response function was also calculated and used in the incremental convolution method, leading exactly to the same results. As in the previous example, the oscillations of the tailpiece side of the string can also be seen in the string–bridge-coupling force.

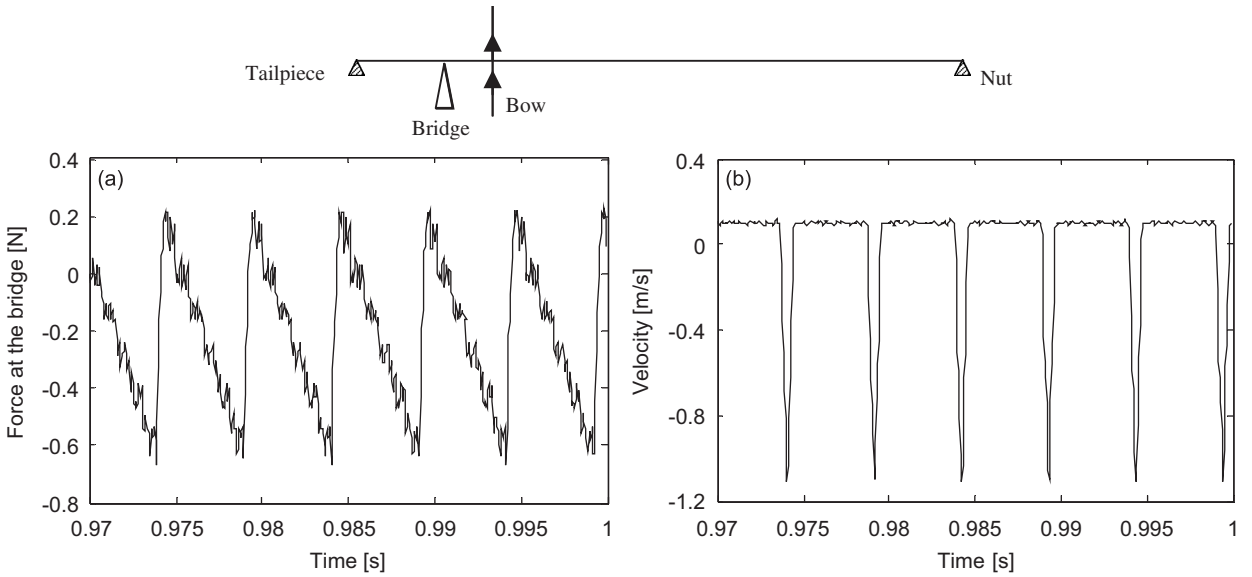

Fig. 11. Force at the bridge and string velocity at the bow contact point for a 0.385 m string pinned at the nut and tailpiece (flexible bridge at 0.330 m, $F_N = 1$ N, $\dot{y}_{\text{bow}} = 0.1$ m s^{-1}).

The similarity of the plots depicted in Figs. 10 and 11 is due to the high impedance presented by the violin bridge to the string waves, which are—in this computation—hardly affected by the comparatively negligible bridge motion. However, it is important to emphasise that this result was obtained when bowing an open G-string, with a fundamental frequency significantly lower than the first body resonance (at about 276 Hz). However, in contrast to this situation, interaction between the string and the body can be much stronger when playing notes with frequencies close to body resonances. Then, bridge motion amplitude (and energy string–body interplaying) may become very significant, as typically experienced in cellos when playing wolf notes. Typically, the cello string suffers a much greater influence from the body, as was clear from the experiments shown in Figs. 5 and 6.

Simulations of plucked violin strings were also performed using a rigidly supported bridge and a flexible (compliant) bridge. Fig. 12(a) and (b) depict the velocity of the string at the plucking point for these two conditions. Using a rigid bridge, case (a), the string motion decreases in a simple exponential manner, while with the compliant bridge, case (b), the interaction with the body dynamics can be clearly seen. In this latter case, energy is transferred from the string and dissipated by the body through the bridge originating a higher motion decay rate. An accurate identification of the damping factor of the individual modal responses of the plucked string, using the modal identification ERA method [40,41], showed that the 0.1% damping of the string modes is unaltered when the string's modal frequencies are not close to a body resonance (the same conclusion applies to the body modes' damping factors). However, in the case of the compliant bridge, when the string and body resonances are close (a few Hertz apart) the string mode damping values become higher, as expected. As an example, the modal damping of the string's second mode (at 392 Hz) couples well to the body's second mode (at 404 Hz) changing the damping value from 0.1% to 0.37%. The correctness of the damping values identified from the time-domain simulations was verified by the complex eigenvalues of a coupled system model, as shown in Appendix A.

5.2. Cello simulation results

As the influence of the cello body on the dynamics of its C_2 string was so apparent during the preliminary experiments, several coupled simulations for this instrument using a modal representation of this instrument body (see Fig. 8) were performed. To easily detect the emergence of a possible wolf note, a glissando was implemented in the simulation scheme by moving a finger along the fingerboard in the range $x_f = 260$–210 mm

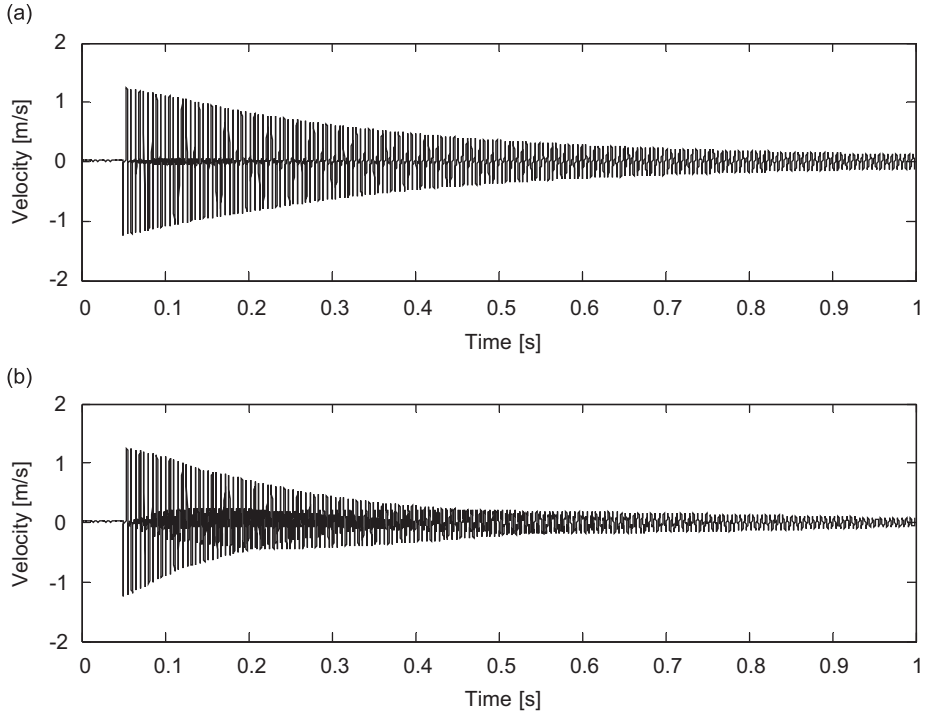

Fig. 12. Simulation of a plucked G-string uncoupled (a) and coupled (b) to the instrument body.

relatively to the bridge—*upward glissando*—or $x_f = 210$–260 mm—*downward glissando*. In this case, the bow was placed at 40 mm from the bridge. To simulate the force exerted by a moving finger on the string, the "finger" was pragmatically modelled using three spring/dashpots of adequate stiffness/dissipation at coordinates $[x_f - 5\,\text{mm}\ ,\ x_f\ ,\ x_f + 5\,\text{mm}]$.

The results are presented in Figs. 13–16, which represent the bridge displacement, for different bowing conditions. The wolf note emerges approximately between positions 243 and 237 mm for the upward glissando, however it does not arise at exactly the same range for the downward glissando as can be seen in Fig. 14.

Another interesting aspect is the fact that the wolf note beating frequency changes for different bowing conditions. Increasing the bowing velocity causes an increase of the beating frequency (Fig. 15), while higher bow normal forces tend to reduce this value. Reducing the bow normal force obviously increases the beating frequency as can be seen in Fig. 16. This latter dependence of the beating frequency on the applied normal force was already briefly numerically demonstrated in Ref. [4]. However, no account has been found in the literature on the bow velocity-dependent beating frequency.

An interesting aspect is that the playing conditions in Figs. 15 and 16 seem to extend the range in which the wolf note emerges, probably associated with the complexity of the body modal response. This feature is also apparent in real-life playing in which musicians denote high difficulty in obtaining clear and repeatable wolf notes.

The explanation of the wolf note formation was first stated by Raman [1] and later revisited by McIntyre and Woodhouse in Ref. [36], which mentions the connection between their time-domain explanation and the frequency-domain explanation by Schelleng. They explain the emergence of the wolf note in the light of the concept of minimum bow force: the continual increase of energy loss from the string due to the build-up of energy in the coupled body implies an increase in the minimum bow force necessary to establish Helmholtz motion. If the minimum bow force needed exceeds the actual bow force, the Helmholtz motion gives way to a "double slip" regime, during which the two slips gradually get out of phase and the new slip takes over as the new Helmholtz motion. This cycle repeats itself giving rise to the characteristic wolf note sound [36].

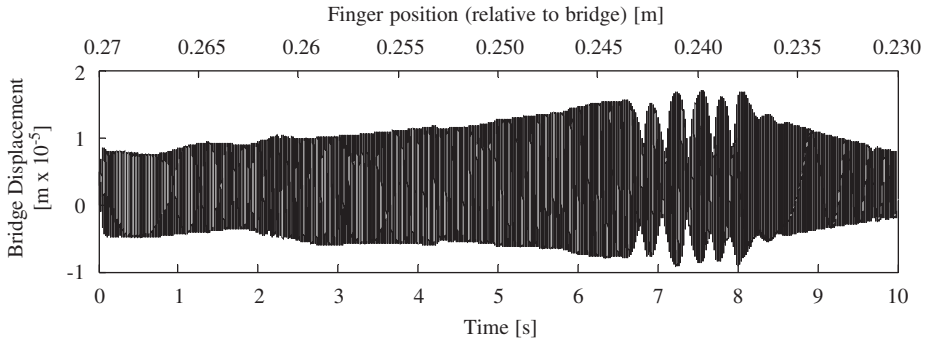

Fig. 13. Simulation of an upward glissando on a cello C-string with $F_N = 2\,\mathrm{N}$ and $\dot{y}_{\mathrm{bow}} = 0.1\,\mathrm{m\,s^{-1}}$.

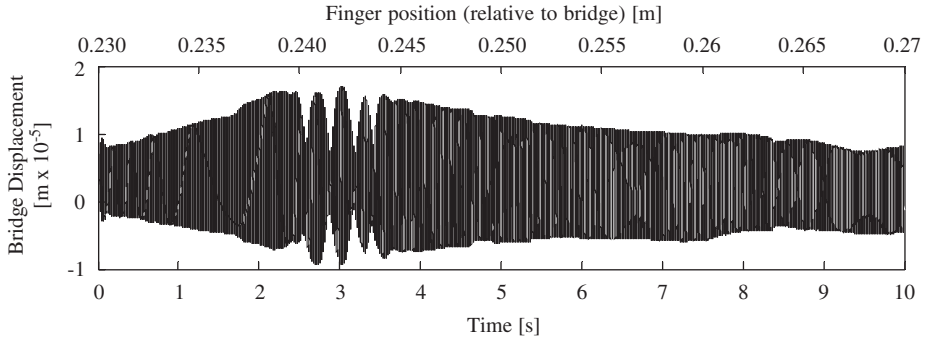

Fig. 14. Simulation of a downward glissando on a cello C-string with $F_N = 2\,\mathrm{N}$ and $\dot{y}_{\mathrm{bow}} = 0.1\,\mathrm{m\,s^{-1}}$.

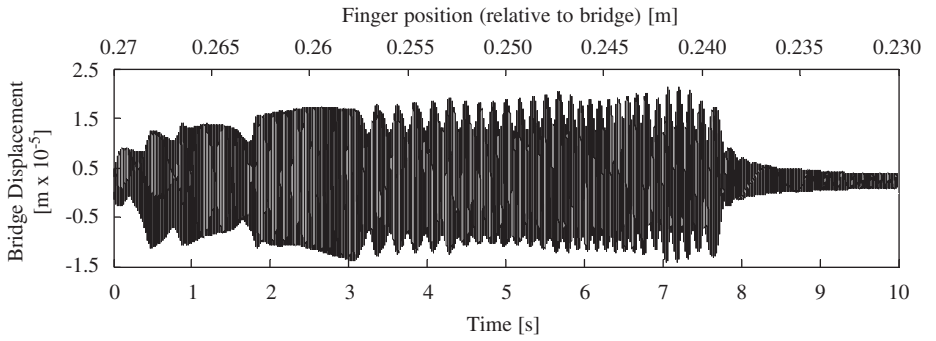

Fig. 15. Simulation of an upward glissando on a cello C-string with $F_N = 2\,\mathrm{N}$ and $\dot{y}_{\mathrm{bow}} = 0.1\,\mathrm{m\,s^{-1}}$.

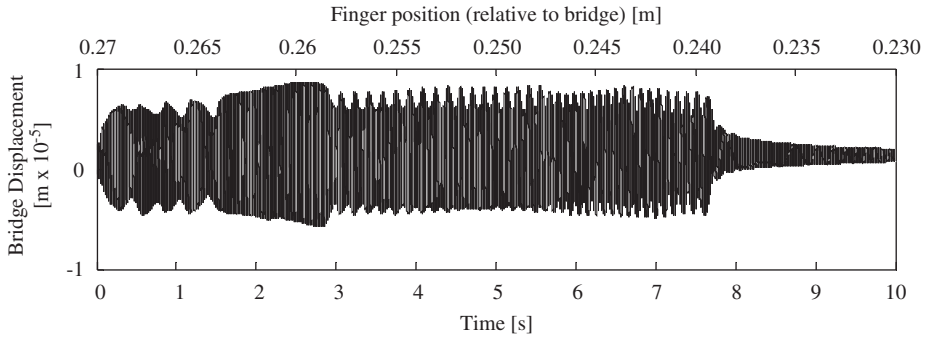

Fig. 16. Simulation of an upward glissando on a cello C-string with $F_N = 4\,\mathrm{N}$ and $\dot{y}_{\mathrm{bow}} = 0.1\,\mathrm{m\,s^{-1}}$.

It is then tempting to link the wolf beating frequency to the conditions enabling the emergence of the double-slip regime. By increasing the normal force double slips will be triggered later (or even suppressed), leading to a lower beating frequency. However, by increasing the bow velocity, double-slip motions will be triggered more easily (as shown in Fig. 19 in this section) causing an increase of the wolf beating frequency. Nevertheless, this tentative reasoning should be supported by a detailed analysis.

In order to map the space of dynamical regimes obtainable with different playing conditions, F_N and $\dot{y}_{\mathrm{bow}}$, at the wolf note finger position, one of these input parameters was successively set to a wide range of discrete values while the other parameter values were continuously increased in an exponential time sweep. It should be clear that this approach is not intended to represent real transient behaviour, but simply parametric changes over a determined range of values (for details on bowed-string musical transients, refer to Guettler [42]).

Fig. 17 shows the instrument bridge displacement time-histories resulting from an exponential sweep of the bow velocity between 0.01 and 1 m s^{-1} while the bow normal force is varied between 0.2 and 10 N in discrete steps proportional to 1, 2 and 5. Fig. 18 represents also the bridge displacement time-histories but now resulting from an exponential sweep of the bow normal force between 0.1 and 10 N while the bow velocity is varied between 0.01 and 0.5 m s^{-1} in the same proportion as in Fig. 17. A colour scheme is used to represent the oscillation regimes that arise for different values of the input parameters.

Six regimes were found during the exponential sweeps performed: a low amplitude or inexistent oscillation; the wolf note regime; the familiar Helmholtz regime; higher-order regimes characterised by multiple slips within one fundamental period; a raucous regime of chaotic oscillations, and, for a small range of input parameters, the anomalous low-frequency regime (see Ref. [43]).

A detailed analysis of the previous figures can give some insight on the mechanism through which musicians usually try to avoid the wolf note by varying the bow-playing conditions. According to these simulations, and as can be seen in Figs. 17 and 18, the wolf note can emerge over a large range of bow velocities and normal

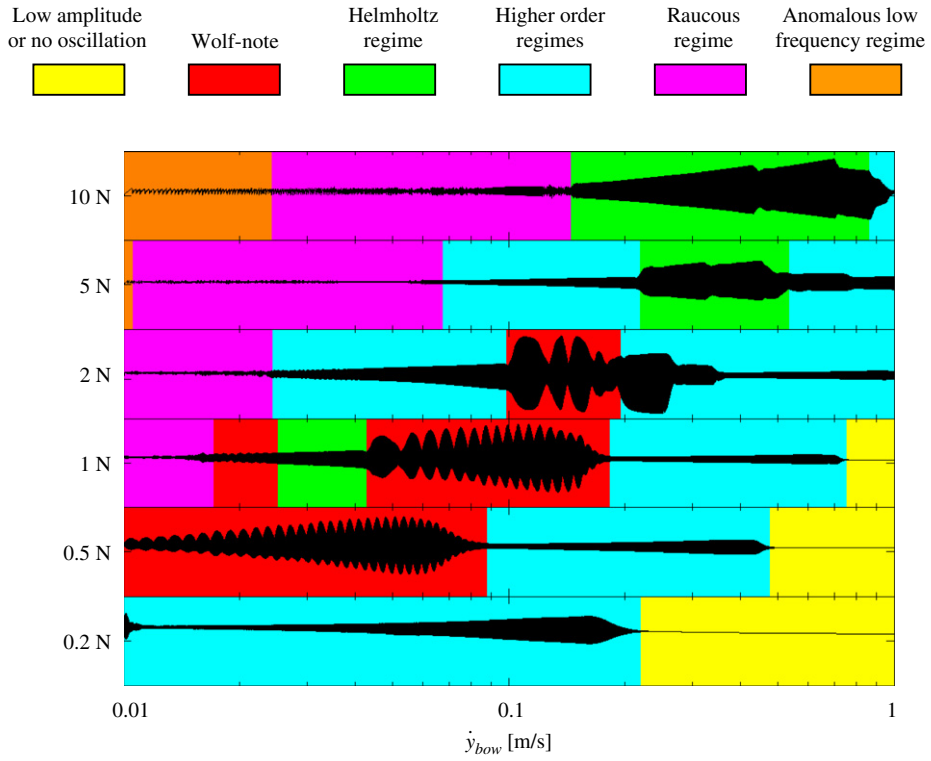

Fig. 17. Map of the oscillation regimes (see legend below) of a cello string bowed at the wolf note position, for discrete values of F_N and an exponential sweep of $\dot{y}_{\mathrm{bow}}$.

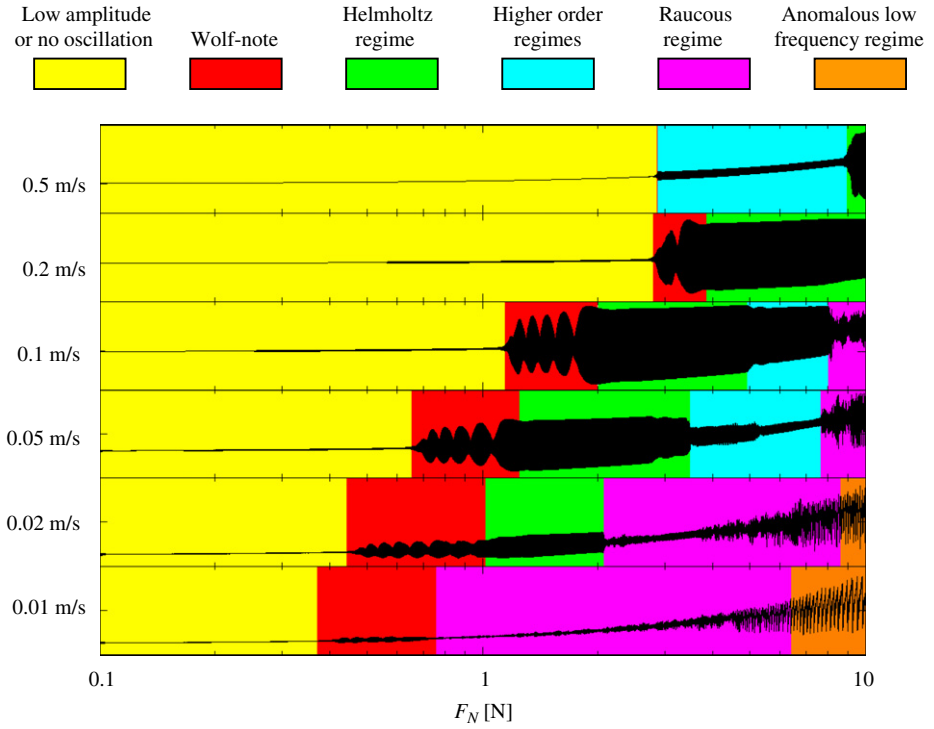

Fig. 18. Map of the oscillation regimes (see legend below) of a cello string bowed at the wolf note position, for discrete values of $\dot{y}_{\mathrm{bow}}$ and an exponential sweep of F_N.

forces. Nevertheless, from Fig. 17, if a bow force of 1 N is applied with a bow velocity around $0.03\,\mathrm{m\,s^{-1}}$, Helmholtz motion is possible, as well as for higher bow velocities and normal forces. Interestingly, Fig. 18 shows a somewhat different picture, with a large range of playing conditions leading to a very low amplitude or even nonexistent oscillation, for values where in Fig. 17 a self-sustained regime would appear. As in many nonlinear systems, various response regimes may arise, for the same driving parameter values, depending on the initial conditions of the motion. Even so, the global behaviour is similar in both figures, with other regimes, such as the anomalous low-frequency, emerging or being less excited, such as the higher-order regime. Thus, it seems probable that musicians try to escape the wolf note by using playing conditions of bow velocity or normal force outside the "wolf" range represented in the previous figures.

Another interesting and expected result is the appearance of the flattening effect [5] when increasing bow normal force is applied. This feature is particularly clear in the results from the force exponential sweep. A detailed analysis (or simply listening to the sound resulting from these simulations) shows that Helmholtz motion is maintained in some regions (see Fig. 18) but as the force increases the fundamental frequency decreases, until chaotic (raucous) motion establishes.

The dependence of the wolf beating frequency on the playing conditions, is also evident in the simulations represented in Figs. 17 and 18. The continuous "sweep" of bow velocity or normal force shows very clearly this dependence. Figs. 19 and 20 depict a detail of the time history of bridge displacement, in which this continuous change in the wolf note frequency is apparent. Values of this frequency are shown for clarity in Figs. 19 and 20.

The values of the wolf note "beating" frequency were identified over short time intervals containing two "beating" periods, represented by the shaded areas in Figs. 19 and 20. As can be seen from the values presented and by inspection of the figures, there is a clear trend for increasing "beating" frequency as the bow velocity increases. Also, as stated before, the opposite effect occurs as the bow normal force is increased.

This variation was also clearly heard in real bowing experience, and for that reason an attempt was made to obtain preliminary experimental results that could qualitatively substantiate the previous numerical

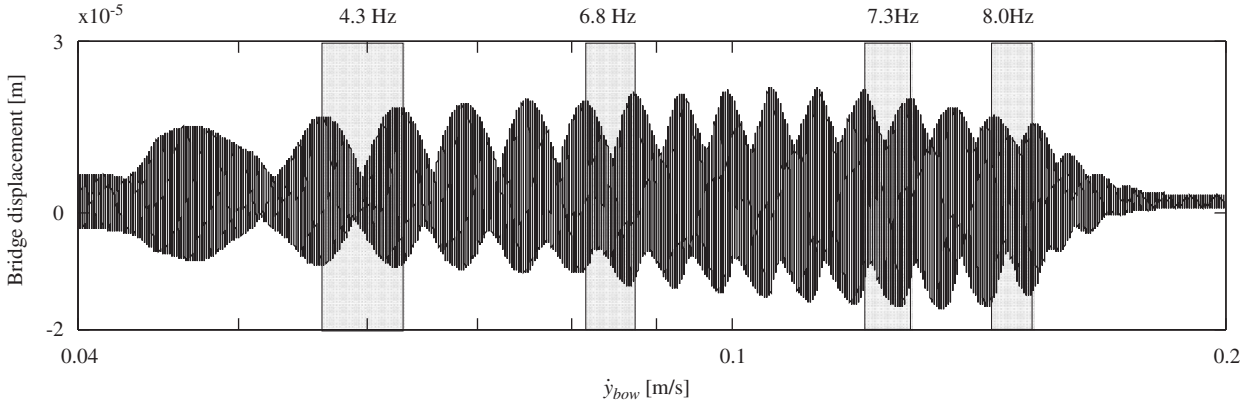

Fig. 19. Detail of the time-history of the cello string oscillation during the wolf note regime played with $F_N = 1$ N with increasing $\dot{y}_{\mathrm{bow}}$.

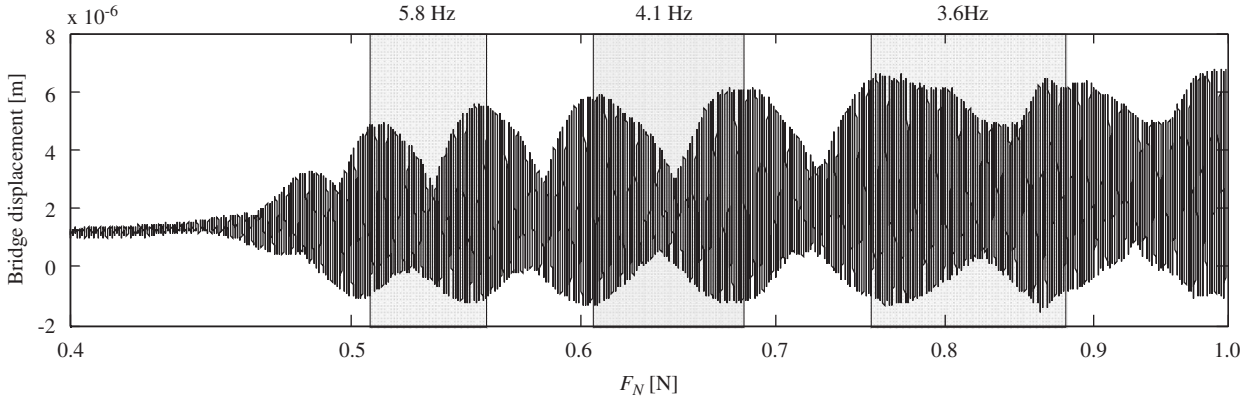

Fig. 20. Detail of the time-history of the cello string oscillation during the wolf note regime played with $\dot{y}_{\mathrm{bow}} = 0.1\ \mathrm{m\,s^{-1}}$, with increasing F_N.

simulations. Obtaining similar controlled playing conditions as the ones numerically implemented was not possible for the scope of this work. Therefore, a human playing approach was followed, and for that reason the qualitative results shown in the figures should be regarded in this light.

Figs. 21 and 22 show the time history of the uncalibrated sound pressure measured at 40 cm from the bridge of a cello (the same that was used to obtain the frequency response in Fig. 3), when playing a wolf note under varying playing conditions. For the results of Fig. 21 an attempt was made to keep the applied normal force constant and continuously increasing (as steady as possible) the bow velocity, while in Fig. 22 the normal force was increased and the velocity kept approximately constant. These results are clear in showing the same trend as in Figs. 19 and 20, apart from some deviations due to the difficulties in accurately controlling the playing parameters.

From the various bow strokes realised during these experiments, other aspects were found which are in accordance (at least qualitatively) with the change in regimes depicted in Figs. 17 and 18. During most of the strokes in which the bow velocity was continuously increased, the wolf note would change to a higher-order regime after a limiting bow velocity (as also seen Fig. 17). On the other hand, the increase of normal force also showed the emergence of the Helmholtz regime after the wolf note, and if the bow force was further increased, the Helmholtz regime would give rise, as expected, to a raucous regime.

6. Conclusions

In this paper, we propose a significant extension of the modal bowed/plucked string modelling technique, in order to incorporate the complex dynamics of real-life instrument bodies, coupled to the string motions.

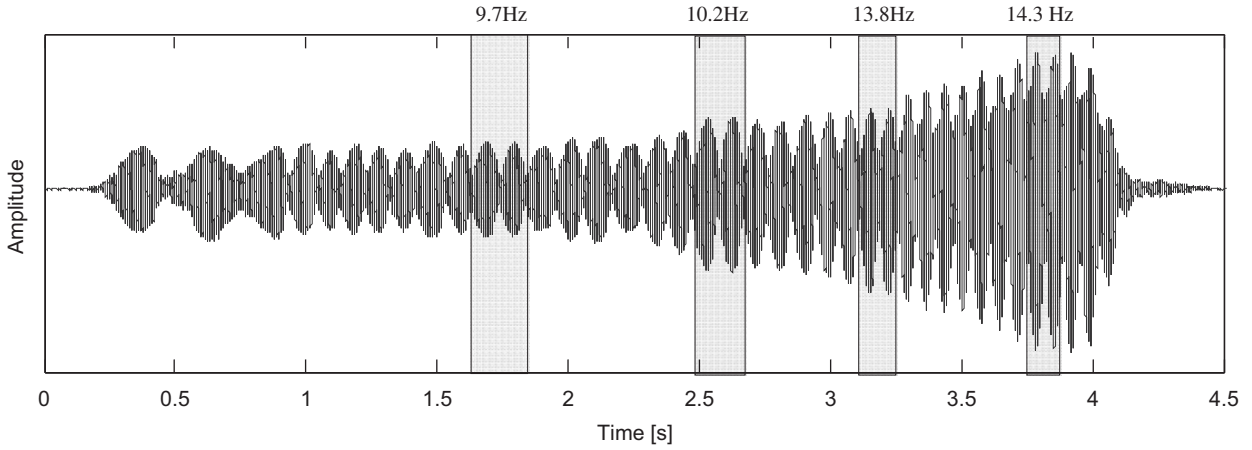

Fig. 21. Measured sound pressure time-history of a wolf note regime played with increasing $\dot{y}_{\mathrm{bow}}$ and approximately constant F_N.

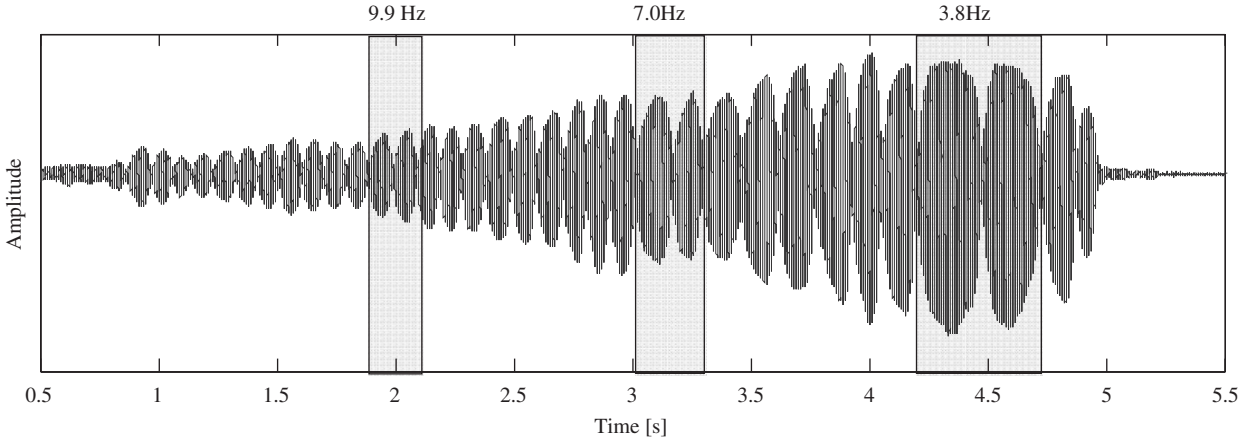

Fig. 22. Measured sound pressure time-history of the wolf note regime played with increasing F_N and approximately constant $\dot{y}_{\mathrm{bow}}$.

In this hybrid approach a modelled string interacts with actual or synthesised body data, in the form of bridge impulse-response functions or identified modes. Numerical simulations illustrate the Helmholtz motions of an isolated and of a body-coupled violin G-string, for comparative boundary conditions. Computations show that string motions between the bridge and the tailpiece may influence, to some degree, the system dynamics. Simulations of a cello C-string subjected to glissando playing highlight the string–body interaction, as well as the interesting behaviour of wolf notes, in particular concerning the dependency of the beating frequency on the bowing parameters.

Acknowledgements

We gladly acknowledge the detailed remarks and criticisms of the anonymous reviewers, which led to a clearer and much improved manuscript.

This work has been endorsed by the Portuguese Fundação para a Ciência e Tecnologia under grant SFRH/BD/12806/2003.

Appendix A. Modal behaviour of the string–body coupled system

Detailed interpretation of the numerical simulations presented in this paper depends on the modal behaviour of the string–body coupled system. Therefore, in this appendix we detail how those coupled modes

may be computed and also present some representative results pertaining to the violin configuration. First, we will address the string constrained by a "rigid" bridge (meaning that $y_b(x_b,t)=0$), and investigate the dependence of the constrained modes on the constraining parameters. Then we focus on the modal behaviour of the full string–body coupled problem, with $y_b(x_b,t)$ given by the body motion at the bridge location, and highlight a few interesting features of the coupled modes.

A.1. String constrained at the bridge

The dynamical behaviour of the string constrained at the bridge is described in terms of Eqs. (2–4) and the constraint force (16) with $y_b(x_b,t)=0$. We obtain

$$[\mathbf{M}]\{\ddot{\mathbf{Q}}(t)\}+[\mathbf{C}]\{\dot{\mathbf{Q}}(t)\}+[\mathbf{K}]\{\mathbf{Q}(t)\}=-\mathbf{C}_{bs}[\Phi(x_b)]\{\dot{\mathbf{Q}}(t)\}-\mathbf{K}_{bs}[\Phi(x_b)]\{\mathbf{Q}(t)\}, \tag{A.1}$$

where, as before, matrices $[\mathbf{M}]=\mathrm{diag}(m_1,\ldots,m_N),[\mathbf{C}]=\mathrm{diag}(2\,m_1\omega_1\,\zeta_1,\ldots,2\,m_N\omega_N\,\zeta_N)$ and $[\mathbf{K}]=\mathrm{diag}(m_1\omega_1^2,\ldots,m_N\omega_N^2)$ pertain to the modal parameters of the unconstrained string, pinned at the tailpiece and the nut, while $\{\mathbf{Q}(t)\}=\langle q_1(t),\ldots,q_N(t)\rangle^{\mathrm{T}}$ is the vector of modal responses. The right-hand-side terms stem from the modal projections (3) of the constraining force (16) at the bridge, accounting for the physical response (4) of the string at the bridge location x_b, whence the coupling matrix

$$[\Phi(x_b)]=\{\varphi_n(x_b)\}\{\varphi_n(x_b)\}^{\mathrm{T}}=\begin{bmatrix}\varphi_1(x_b)\varphi_1(x_b) & \varphi_1(x_b)\varphi_2(x_b) & \ldots & \varphi_1(x_b)\varphi_N(x_b)\\ \varphi_2(x_b)\varphi_1(x_b) & \varphi_2(x_b)\varphi_2(x_b) & \ldots & \varphi_2(x_b)\varphi_N(x_b)\\ \vdots & \vdots & \ddots & \vdots\\ \varphi_N(x_b)\varphi_1(x_b) & \varphi_N(x_b)\varphi_2(x_b) & \ldots & \varphi_N(x_b)\varphi_N(x_b)\end{bmatrix}, \tag{A.2}$$

where $\{\varphi_n(x_b)\}\equiv\langle\,\varphi_1(x_b)\quad\varphi_2(x_b)\quad\ldots\quad\varphi_N(x_b)\,\rangle^{\mathrm{T}}$ stands for the modeshapes, at the bridge location, of the unconstrained string.

From Eq. (A.1) we obtain

$$[\mathbf{M}]\{\ddot{\mathbf{Q}}(t)\}+[[\mathbf{C}]+C_{bs}[\Phi(x_b)]]\{\dot{\mathbf{Q}}(t)\}+[[\mathbf{K}]+K_{bs}[\Phi(x_b)]]\{\mathbf{Q}(t)\}=\{0\}. \tag{A.3}$$

And, assuming free-response solutions of the form $\{\mathbf{Q}(t)\}=\{\Psi_n^Q\}\exp(\lambda_n t)$, the following quadratic eigenproblem is obtained:

$$\left[\lambda_n^2[\mathbf{M}]+\lambda_n[[\mathbf{C}]+C_{bs}[\Phi(x_b)]]+[[\mathbf{K}]+K_{bs}[\Phi(x_b)]]\right]\{\Psi_n^Q\}=\{0\} \tag{A.4}$$

which can be easily converted into an equivalent first-order (state-space) form and then readily solved using standard procedures. Eq. (A.5) is one possible symmetrical form, among others (see, for instance Ref. [44]).

$$\left(\lambda_n\begin{bmatrix}[[\mathbf{C}]+C_{bs}[\Phi(x_b)]] & [\mathbf{M}]\\ [\mathbf{M}] & [0]\end{bmatrix}+\begin{bmatrix}[[\mathbf{K}]+K_{bs}[\Phi(x_b)]] & [0]\\ [0] & -[\mathbf{M}]\end{bmatrix}\right)\begin{Bmatrix}\{\Psi_n^Q\}\\ \lambda_n\{\Psi_n^Q\}\end{Bmatrix}=\begin{Bmatrix}\{0\}\\ \{0\}\end{Bmatrix} \tag{A.5}$$

The eigenvalues and corresponding eigenvectors obtained from (A.5) are in general complex and, for oscillating solutions, arise in conjugate pairs $\lambda_n=\hat{\sigma}_n\pm\mathrm{i}\hat{\omega}_n$. The (damped) modal frequencies $\hat{\omega}_n=\mathrm{Im}(\lambda_n)$ and modal dissipation values $\hat{\sigma}_n=\mathrm{Re}(\lambda_n)$ reflect the linear dynamics of the dissipative-coupled system, in terms of the constraint parameters K_{bs} and C_{bs}. The undamped modal frequencies $\hat{\omega}_{n0}$ and modal damping values $\hat{\zeta}_n$ of the constrained string may be inferred from the various λ_n using the following relations:

$$\hat{\omega}_{n0}=\sqrt{\hat{\sigma}_n^2+\hat{\omega}_n^2},\quad \hat{\zeta}_n=-\frac{\hat{\sigma}_n}{\sqrt{\hat{\sigma}_n^2+\hat{\omega}_n^2}}, \tag{A.6}$$

and one obtains $\hat{\omega}_n=\hat{\omega}_{n0}\sqrt{1-\hat{\zeta}_n^2}$, as usual. After obtaining the eigenvectors $\{\Psi_n^Q\}$ of the coupled system in terms of the modal amplitude coefficients of the original string modes, one can easily express the corresponding modeshapes $\{\Psi_n^Y\}$ in terms of physical amplitudes by recombination of the unconstrained modeshapes

$$\{\Psi_n^Y\}=[\{\varphi_1\},\{\varphi_2\},\ldots,\{\varphi_N\}]\{\Psi_n^Q\},\quad n=1,2,\ldots,N. \tag{A.7}$$

Figs. A1 and A2 show the changes in the string modal frequencies and damping values, respectively, as the bridge constraining stiffness K_{bs} increases in the range 10–$10^7\,\mathrm{Nm}^{-1}$ with no coupling dissipation ($C_{bs}=0$), for the first nine modes. One may notice that modal frequencies behave as an almost harmonic series for the very lowest values of K_{bs}, meaning that the bridge is then barely "felt" by the string. On the opposite extreme, when $K_{bs}>10^6\,\mathrm{Nm}^{-1}$, further increase in the constraining stiffness brings no significant changes, as for all practical purposes, the bridge is already "rigid" as far as the string is concerned. Again, the highly constrained string modal frequencies are almost harmonic, except for a mode at 1224 Hz, which will be explained later. All the modal frequencies increase with K_{bs}, as they should, system inharmonicity being maximal at about $K_{bs}\simeq 5\times 10^3\,\mathrm{N\,m}^{-1}$, when the bridge is far from "rigid" but already a significant constraint.

From Fig. A2 it appears that the modal damping values of the constrained modes are almost independent K_{bs} when $C_{bs}=0$, and always slightly lower than those of the original (unconstrained) string modes (here 0.1% was postulated for all modes). However, as shown in Fig. A3, the scenario is considerably different when C_{bs} is not nil (here $C_{bs}=10\,\mathrm{Ns\,m}^{-1}$), because significant energy is then damped out when the constraining stiffness is low enough to allow for string motions at the bridge location. Notice that, for high values $K_{bs}>10^6\,\mathrm{N\,m}^{-1}$, modal damping of the constrained modes does not depend on C_{bs} and only reflect the modal damping values of the original modes.

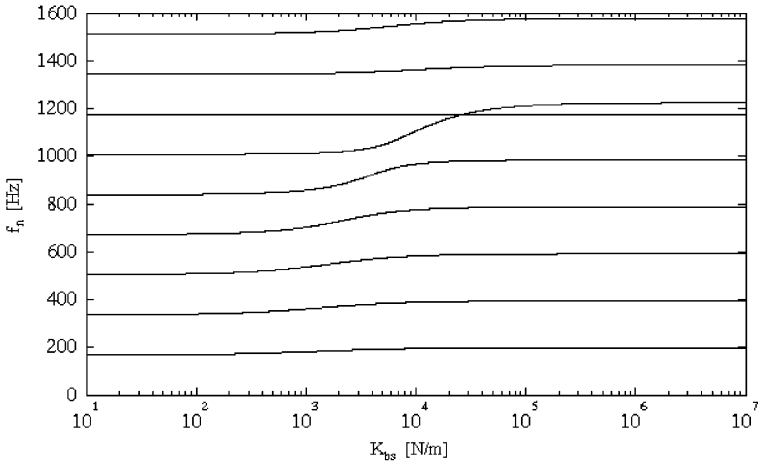

Fig. A1. Modal frequencies of the string modes constrained at the bridge, as a function of the stiffness coupling constant K_{bs} (with $C_{bs}=0$).

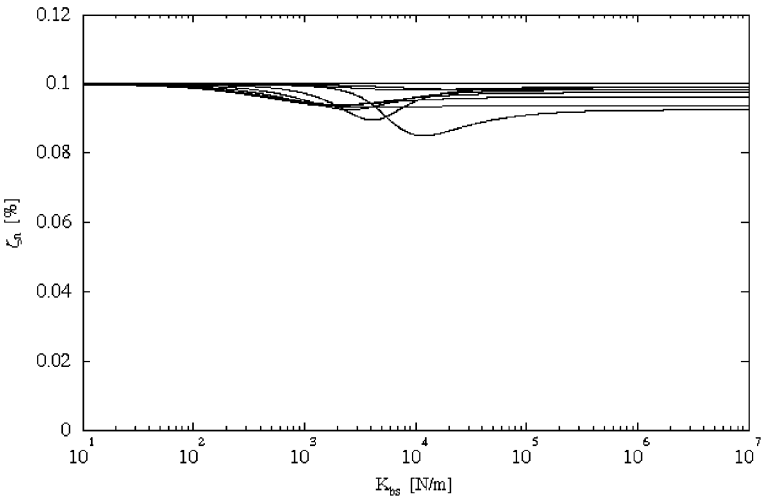

Fig. A2. Modal damping of the string modes constrained at the bridge, as a function of the stiffness coupling constant K_{bs} (with $C_{bs}=0$).

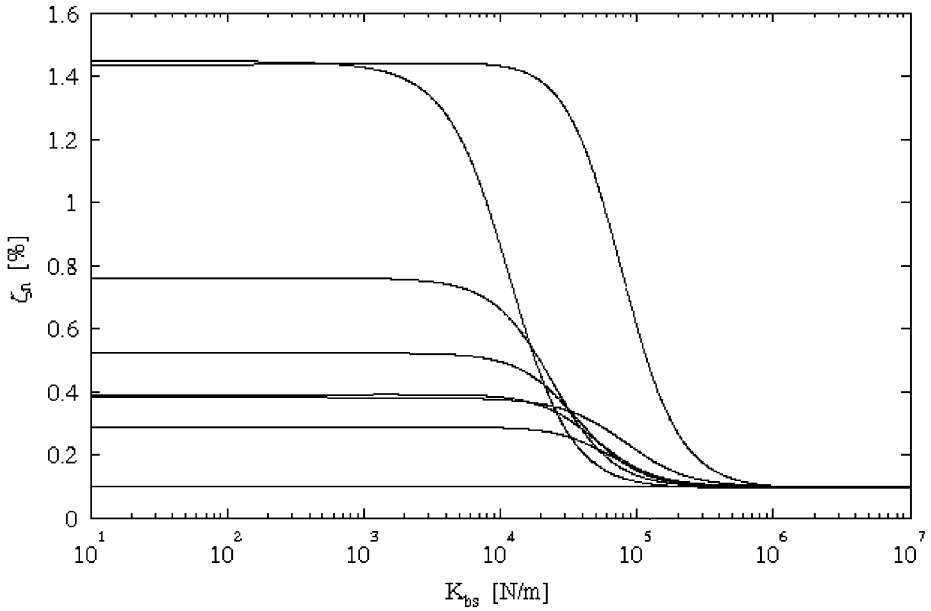

Fig. A3. Modal damping of the string modes constrained at the bridge, as a function of the stiffness coupling constant K_{bs} (with $C_{bs} = 10\,\mathrm{N\,s\,m^{-1}}$).

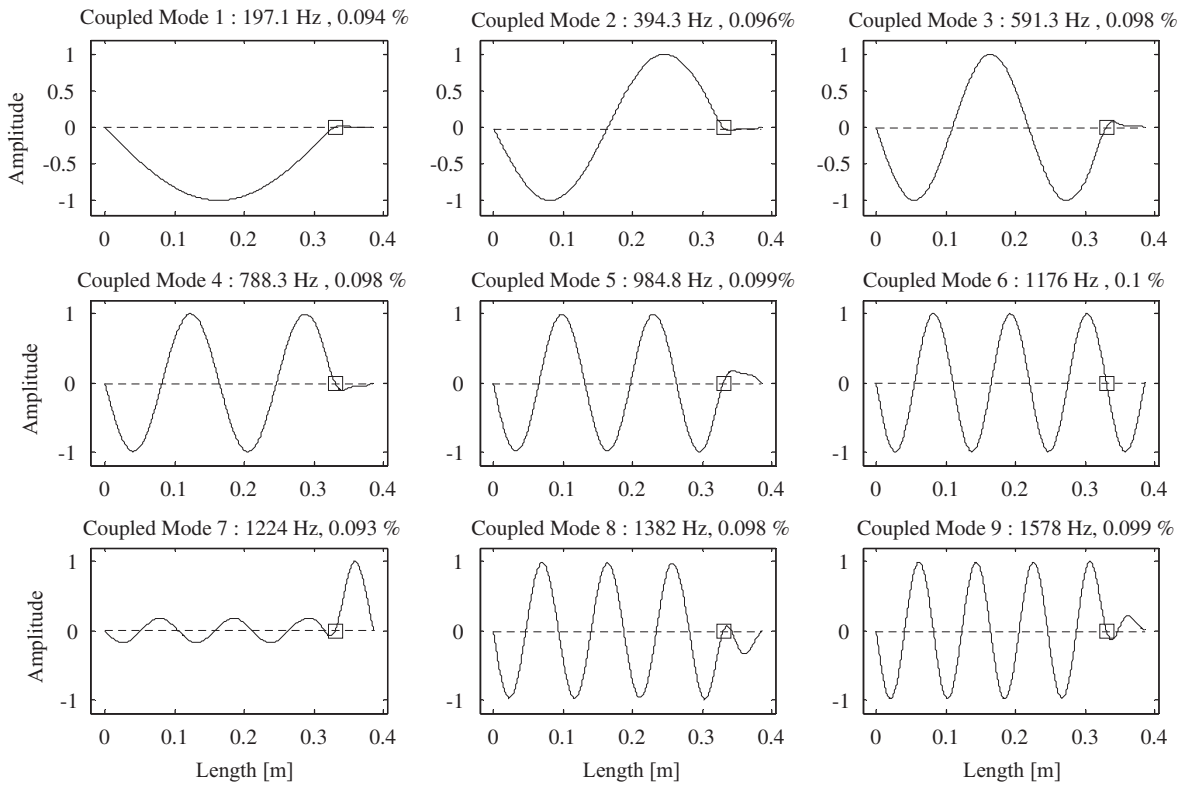

Fig. A4. Modeshapes of the first string modes constrained at an almost-rigid bridge ($K_{bs} = 10^7\,\mathrm{N\,m^{-1}}$).

To conclude this section Fig. A4 displays the modeshapes of the first nine constrained modes, computed from (A.5) and (A.7), when the bridge behaves as an almost-rigid constraint ($K_{bs} = 10^7\,\mathrm{N\,m^{-1}}$). Note that for most modes in this frequency range the modal amplitudes are only significant between the nut and the bridge, the string length between the bridge and the tailpiece being only marginally active, which is well consistent with the near-harmonic series obtained for the constrained modal frequencies. The only exceptions (in this frequency range) being the 6th mode, with its modal frequency barely affected by the string motion on the tailpiece side (because the bridge naturally stands at a node), and mostly the 7th mode. Indeed, this mode is strongly dominated by a localized tailpiece-side response, and hence displays a modal frequency mostly related to the bridge-tailpiece distance. Obviously, this is the mode which breaks the harmonic series of the modal frequencies displayed by the right-hand side of Fig. A1.

A.2. String–body coupled modes

We will now address in a similar manner the coupled modes of the string–body system. Formulation follows lines similar to the previous presentation, although—because now we have $y_b(x_b,t)\neq 0$—the modal parameters of the P body modes must obviously be included. Then, from Eqs. (2)–(4) and (14)–(16), we obtain the coupled system

$$\begin{bmatrix} \mathbf{M} & 0 \\ 0 & \mathbf{M}_B \end{bmatrix} \begin{Bmatrix} \{\ddot{\mathbf{Q}}(t)\} \\ \{\ddot{\mathbf{Q}}_B(t)\} \end{Bmatrix} + \begin{bmatrix} \mathbf{C} & 0 \\ 0 & \mathbf{C}_B \end{bmatrix} \begin{Bmatrix} \{\dot{\mathbf{Q}}(t)\} \\ \{\dot{\mathbf{Q}}_B(t)\} \end{Bmatrix} + \begin{bmatrix} \mathbf{K} & 0 \\ 0 & \mathbf{K}_B \end{bmatrix} \begin{Bmatrix} \{\mathbf{Q}(t)\} \\ \{\mathbf{Q}_B(t)\} \end{Bmatrix}$$
$$= -C_{bs} \begin{bmatrix} \Phi_{SS}(x_b) & \Phi_{SB}(x_b) \\ \Phi_{BS}(x_b) & \Phi_{BB}(x_b) \end{bmatrix} \begin{Bmatrix} \{\dot{\mathbf{Q}}(t)\} \\ \{\dot{\mathbf{Q}}_B(t)\} \end{Bmatrix} - K_{bs} \begin{bmatrix} \Phi_{SS}(x_b) & \Phi_{SB}(x_b) \\ \Phi_{BS}(x_b) & \Phi_{BB}(x_b) \end{bmatrix} \begin{Bmatrix} \{\mathbf{Q}(t)\} \\ \{\mathbf{Q}_B(t)\} \end{Bmatrix} \tag{A.8}$$

with the coupling sub-matrices

$$\begin{aligned} [\Phi_{SS}(x_b)] &= \{\varphi_n(x_b)\}\{\varphi_n(x_b)\}^{\mathrm{T}}; \quad [\Phi_{SB}(x_b)] = -\{\varphi_n(x_b)\}\{\phi_p(x_b)\}^{\mathrm{T}}, \\ [\Phi_{BS}(x_b)] &= -\{\phi_p(x_b)\}\{\varphi_n(x_b)\}^{\mathrm{T}}; \quad [\Phi_{BB}(x_b)] = \{\phi_p(x_b)\}\{\phi_p(x_b)\}^{\mathrm{T}}, \end{aligned} \tag{A.9}$$

where $\{\phi_p(x_b)\}$ is the vector of the body modeshape values at the bridge location (here taken as unity, following the normalization procedure adopted).

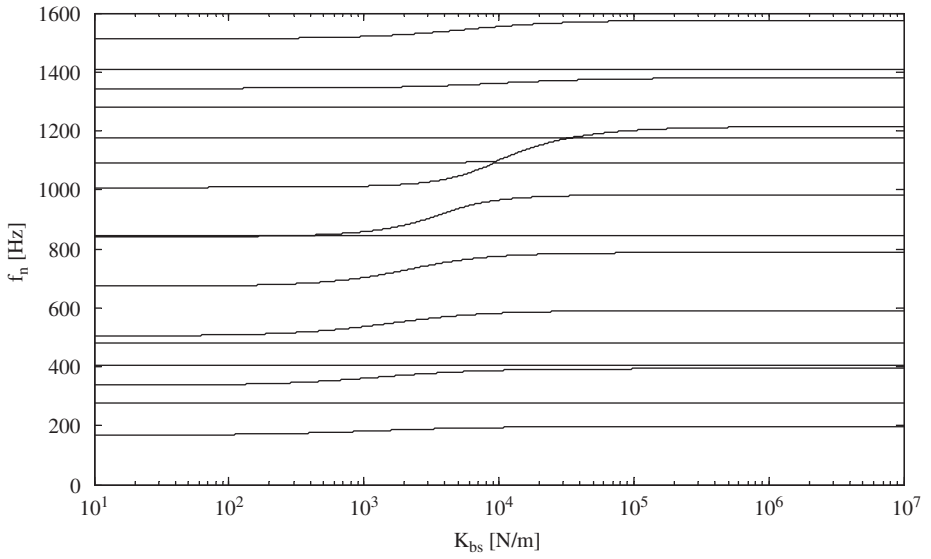

Fig. A5. Modal frequencies of the string–body coupled modes, as a function of the stiffness coupling constant K_{bs} at the bridge (with $C_{bs} = 0$).

Eq. (A.8) is of the form (A.1), although obviously the system size is now $N+P$. Therefore, the corresponding eigenproblem may also be written in form (A.4) or (A.5), from which the string–body coupled modes are computed. Notice that the coupling matrix built from Eq. (A.9) is symmetric, as it should be. This, however, is no guarantee that the coupled modes will display real modeshapes—and indeed, as will be shown later, complex modes are the rule here more than the exception.

Fig. A.5 displays the change of the string–body modal frequencies as the stiffness-coupling constant K_{bs} increases. These computations are based on the same unconstrained string modes as before, while Table A1 presents the modal frequencies and damping values used for the first few body modes used in this calculation. Notice that these body modes display damping values typically one order of magnitude higher than the uncoupled string modes.

Essentially, the left-hand side of the plot shows the string and body modes when they are almost uncoupled, while the right-hand side of the plot shows the string and body almost rigidly coupled at the bridge. In-between, the interplay of the modal frequencies stems from increasing coupling. Understandably, the

Table A1
Body first modal frequencies and damping values

Mode	1	2	3	4	5
Frequency (Hz)	276.5	404.0	480.7	846.5	1093.0
Damping (%)	2	3	1	1	1

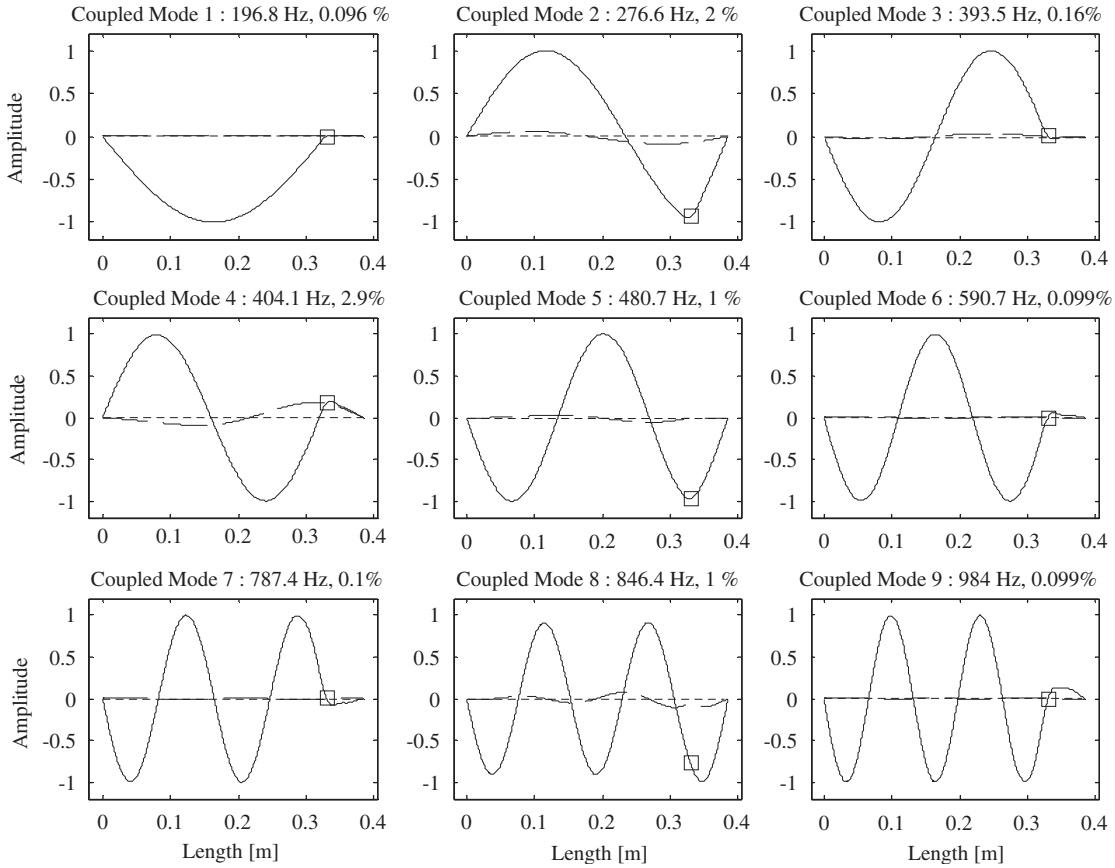

Fig. A6. Complex modeshapes of the first string–body coupled modes ($K_{bs} = 10^7\,\mathrm{N\,m^{-1}}$).

string modal frequencies change significantly as K_{bs} increases, while the body modal frequencies are hardly affected.

At the modal frequencies controlled by the body, the bridge presents a lower impedance to the string, so that the coupled modes do not display any more a node at the bridge location. This is demonstrated in Fig. A6, which shows the first 9 modes of the coupled system (using $K_{bs} = 10^7\,\mathrm{Nm}^{-1}$)—see modes 2, 4, 5 and 8. Also notice that, the coupled string–body modes are complex, as the energy dissipation from the string will be mainly localized at the bridge, and hence damping is nonproportional. This is particularly significant for the coupled modes controlled by the body motion, as shown in Fig. A6, where the modeshapes have been normalised at unity for the maxima of their real part, the corresponding imaginary part being plotted with a dotted line.

Concerning the modal damping of the coupled modes one may note that, when the bridge is almost still, the modal damping values are essentially those of the uncoupled string modes. Also understandably, when the coupled modes are controlled by the body, damping values are essentially those of the corresponding body modes. As thoroughly discussed by Woodhouse [15], if the system damping is modelled in a satisfying manner, such typical scenario should be displayed even when two coupled "string-controlled" and "body-controlled" modes present close frequencies, as the orders of magnitude of their respective damping values should respect those of the decoupled substructures. An illustration is provided by modes 3 and 4 in Fig. A6, even so, the 60% damping increase in the "string-controlled" mode is enough to produce some of the visible changes in the response shown in Fig. 12(b). A more detailed discussion of the string–body coupled responses is postponed to a forthcoming paper.

References

[1] C.V. Raman, On the mechanical theory of the vibrations of bowed strings and of musical instruments of the violin family, with experimental verification of the results, *Indian Association for the Cultivation of Science* 15 (1918) 1–158.

[2] F.G. Friedlander, On the oscillations of the bowed string, *Proceedings of the Cambridge Philosophical Society* 49 (1953) 516–530.

[3] J.C. Schelleng, The bowed string and the player, *Journal of the Acoustical Society of America* 53 (1973) 26–41.

[4] M.E. McIntyre, R.T. Schumacher, J. Woodhouse, On the oscillations of musical instruments, *Journal of the Acoustical Society of America* 74 (1983) 1325–1345.

[5] L. Cremer, *The Physics of the Violin*, MIT Press, Cambridge, MA, 1984.

[6] L. Meirovich, *Principles and Techniques of Vibrations*, Prentice-Hall International, New Jersey, 1997.

[7] F. Axisa, P. Trompette, *Modelling Mechanical Systems (Volume 2)—Structural Elements*, Elsevier, Oxford, 2005.

[8] J. Antunes, M.G. Tafasca, L.L. Henrique, Simulation of the Bowed-String Dynamics: Part 1—A Nonlinear Modal Approach, Proceedings of the 5th French Acoustics Congress, Lausanne, September 2000.

[9] M.G. Tafasca, J. Antunes, L.L. Henrique, Simulation of the bowed-string dynamics: part 2—parametric computations, *Proceedings of the fifth French Acoustics Congress*, Lausanne, September 2000.

[10] J. Antunes, L.L. Henrique, O. Inácio, Aspects of bowed-string dynamics, *Proceedings of the seventeenth International Congress on Acoustics*, Rome, 2001.

[11] O. Inácio, Largeur d'Archet et Régimes Dynamiques de la Corde Frottée, *Proceedings of the sixth French Acoustics Congress*, Lille, 2002.

[12] J. Puaud, R. Caussé, V. Gibiat, Quasi-périodicité et bifurcations dans la note de loup, *Journal of Acoustique* 4 (1991) 253–259.

[13] P. Huang, S. Serafin, J.O. Smith, A waveguide mesh model of high-frequency violin body resonances, *Proceedings of the International Computer Music Conference (ICMC 2000)*, Berlin, August 27–September 1, 2000, pp. 86–89.

[14] G. Derveaux, A. Chaigne, P. Joly, E. Bécache, Time-domain simulation of a guitar: model and method, *Journal of the Acoustical Society of America* 114 (2003) 3368–3383.

[15] J. Woodhouse, On the synthesis of guitar plucks, *Acta Acustica United with Acustica* 90 (2004) 928–944.

[16] R.R. Craig, *Structural Dynamics*, Wiley, New York, 1981.

[17] N. Fletcher, T. Rossing, *The Physics of Musical Instruments*, second ed., Springer, New York, 2005 (re-issued).

[18] D. Beeman, Some multistep methods for use in molecular dynamics calculations, *Journal of Computational Physics* 20 (1976) 130–139.

[19] E. Rabinowicz, *Friction and Wear of Materials*, Wiley, New York, 1965.

[20] I. Kragelsky, M. Dobychin, V. Kombalov, *Friction and Wear: Calculation Methods*, Pergamon Press, Oxford, 1982.

[21] J. Oden, J. Martins, Models and computational methods for dynamic friction phenomena, *Computer Methods in Applied Mechanics* 50 (1983) 67–76.

[22] D.A. Haessig Jr., B. Friedland, On the modelling and simulation of friction, *Measurements and Control Journal of Dynamic Systems* 107 (1985) 100–103.

[23] D. Karnopp, Computer simulation of stick-slip friction in dynamic systems, *Measurement and Control ASME Journal of Dynamic Systems* 50 (1983) 67–76.

[24] R.I. Leine, D.H. van Campen, A. de Kraker, L. van den Steen, Stick-slip vibrations induced by alternate friction models, *Nonlinear Dynamics* 16 (1998) 41–54.
[25] J. Antunes, F. Axisa, B. Beaufils, D. Guilbaud, Coulomb friction modelling in numerical simulations of vibration and wear work rate of multispan tube bundles, *Journal of Fluids and Structures* 4 (1990) 287–304.
[26] H. Lazarus, Die Behandlung der Selbsterregten Kippschwingungen der Gestrichenen Saite mit Hilfe der Endlichen Laplace Transformation, Dissertation, Tech. Univ. Berlin 1972.
[27] J.H. Smith, J. Woodhouse, The tribology of rosin, *Journal of the Mechanics and Physics of Solids* 48 (2000) 1633–1681.
[28] O. Inácio, L. Henrique, J. Antunes, The dynamics of Tibetan singing bowls, *Acta Acustica United with Acustica* 92 (2006) 637–653.
[29] W.C. Swope, H.C. Andersen, P.H. Berens, K.R. Wilson, A computer simulation method for the calculation of equilibrium constants for the formulation of physical clusters of molecules: application to small water clusters, *Journal of Chemical Physics* 76 (1982) 637–649.
[30] P. Deuflhard, J. Hermans, B. Leimkuhler, A.E. Mark, S. Reich, R.D. Skeel (Eds.), *Computational Molecular Dynamics: Challenges, Methods, Ideas-Series: Lecture Notes in Computational Science and Engineering*, Vol. 4, Springer, Berlin, 1999.
[31] N.M. Newmark, A method of computation for structural dynamics, *ASCE Journal of the Engineering Mechanics Division* 85 (1959) 67–94.
[32] K.J. Bathe, E.L. Wilson, Stability and accuracy analysis of direct integration methods, *Earthquake Engineering and Structural Dynamics* 1 (1973) 283–291.
[33] J. Schelleng, The violin as a circuit, *Journal of the Acoustical Society of America* 35 (1963) 326–338.
[34] I.M. Firth, J.M. Buchanan, The wolf in the cello, *Journal of the Acoustical Society of America* 53 (1973) 457–463.
[35] H. Benade, The wolf tone on violin family instruments, *Catgut Acoustical Society Newsletter* 24 (1975) 21–23.
[36] M.E. McIntyre, J. Woodhouse, On the fundamentals of bowed-string dynamics, *Acustica* 43 (1979) 93–108.
[37] C. Gough, The resonant response of a violin G-string and the excitation of the wolf note, *Acustica* 44 (1980) 113–123.
[38] J. Woodhouse, On the playability of violins: part 2—minimum bow force and transients, *Acustica* 78 (1993) 137–153.
[39] E. Jansson, Acoustics for Violin and Guitar Makers: chap. 4—Properties of the Violin and Guitar String, fourth ed., 2002, online at ⟨http://www.speech.kth.se/music/acviguit4⟩.
[40] J.N. Juang, R.S. Pappa, An eigensystem realization algorithm for modal parameter identification and model reduction, *Journal of Guidance, Control, and Dynamics* 8 (5) (1985) 620–627.
[41] J.N. Juang, *Applied System Identification*, Prentice-Hall PTR, New Jersey, 1994.
[42] K. Guettler, A. Askenfelt, Acceptance limits for the duration of pre-Helmholtz transients in bowed string attacks, *Journal of the Acoustical Society of America* 101 (1997) 2903–2913.
[43] R.J. Hanson, A.J. Schneider, F.W. Halgedahl, Anomalous low-pitched tones from a bowed violin string, *Catgut Acoustical Society Journal* 2 (No. 6, Series II) (1994).
[44] A.F. Bertolini, Review of eigensolution procedures for linear dynamic finite element analysis, *Applied Mechanics Reviews* 51 (1998) 155–172.